FABRICATION AND CHARACTERIZATION OF EPITAXIAL GRAPHENE NANORIBBON TRANSPORT DEVICES

A Dissertation
Presented to
The Academic Faculty

by

Owen Vail

In Partial Fulfillment
of the Requirements for the Degree
Doctor of Philosophy in the
School of Physics

Georgia Institute of Technology
May 2017

FABRICATION AND CHARACTERIZATION OF EPITAXIAL GRAPHENE NANORIBBON TRANSPORT DEVICES

Approved by:

Dr. Zhigang Jiang, Advisor
School of Physics
Georgia Institute of Technology

Dr. Claire Berger
School of Physics
Georgia Institute of Technology

Dr. Walter A. de Heer
School of Physics
Georgia Institute of Technology

Dr. Azad J. Naeemi
School of Electrical and Computer Engineering
Georgia Institute of Technology

Dr. Phillip N. First
School of Physics
Georgia Institute of Technology

Date to be Approved: 2/23/2017

To my parents,

Stephen Vail and Gail Forsyth-Vail,

For their unending love and support

ACKNOWLEDGEMENTS

First and foremost, I wish to thank my advisor, Dr. Zhigang Jiang. His guidance and understanding has been instrumental to all the projects we have explored together over these past years. I would also like to thank my committee, many of whom I had the pleasure of working extensively with: Dr. Walt A. de Heer, Dr. Phillip N. First, Dr. Claire Berger, and Dr. Azad Naeemi. I also appreciate the opportunity for collaboration with Dr. Edward Conrad and Dr. Lei Ma.

I am grateful to my colleagues for their help and comradery: Yuxuan Jiang, Dr. Wenlong Yu, Dr. Xuchi Chen, Dr. Chao Huan, Dr. Anton Sidorov, Anna Miettinen, Jeremy Yang, Meredith Nieves, Di Chen, Jean-Phillippe Turmaud, Jamey Gigliotti, Yiran Hu, Dogukan Deniz. I especially want to thank Dr. John Hankinson and everyone in the deHeer research group for developing a novel material worthy of further research: Dr. Zelei Guo, Dr. James Palmer, Dr. Ming Ruan, Dr. Yike Hu, Dr. Michael Sprinkle.

Finally, I give my sincere appreciation for all my friends and family that have been there for me throughout my life.

TABLE OF CONTENTS

LIST OF TABLES

LIST OF FIGURES

LIST OF SYMBOLS AND ABBREVIATIONS

2-D	Two Dimensional
GNR	Graphene Nanoribbon
SiC	Silicon Carbide
epiGNR	Epitaxial Graphene Nanoribbon
Al	Aluminum
Au	Gold
Pd	Palladium
Co	Cobalt
Al_2O_3	Aluminum Oxide
IPA	Isopropyl Alcohol
NPGS	Nanometer Pattern Generation System
SEM	Scanning Electron Microscopy
RIE	Reactive Ion Etching
AFM	Atomic Force Microscopy
EFM	Electronic Force Microscopy
LFM	Lateral Force Microscopy
RPE	Reverse Proximity Effect
BTK	Blonder-Tinkham-Klapwijk
AC	Alternating Current
DC	Direct Current
CNP	Charge Neutrality Point

SUMMARY

Patterned growth of epitaxial graphene has piqued the interest of the scientific community by revealing an interesting structure with a lot of potential: the sidewall nanoribbon. Epitaxial graphene is produced by confinement-controlled sublimation of silicon carbide. With the right growth conditions, graphene on the silicon face will be confined to topographical steps on the surface. The nanoribbon produced in this fashion is of high quality with crystallographic edges and few defects. Its transport properties, such as mobility and mean free path, are competitive with industrial transmission lines.

Fabrication of mesoscopic devices for experimental transport physics can be challenging and require novel design solutions. Electron beam lithography provides the desired resolution for nanopatterned circuits and electron beam evaporation allows for high quality metallization without damaging the graphene ribbon. Plasma etching is used to define the sidewalls and purge the device area. While many of the devices in this dissertation were made using these techniques, other advanced techniques are also explored, such as shadow mask evaporation and multi-step photolithography.

In this dissertation, I will examine the transport properties of epitaxial graphene nanoribbon and its potential for use as a property-rich transmission line. Two directions of experimentation are taken: the first focuses on the superconducting proximity effect and the second on the electrical noise in response to a gate. These experiments reflect the diversity in properties held by the sidewall structure, with one aiming to explore the spin-polarization of the ribbon and the other focused on more traditional electronic transport and use of the ribbon for competitive integrated electronics.

CHAPTER 1. INTRODUCTION

1.1 Transport Physics

Many forms of transport physics can be parameterized by the length scales over which a carrier maintains information about a particular physical property. This length scale is determined by the distance between scattering events that randomize the carrier's state with regards to the property of interest. This section will focus on the mean free path and will build the theory of ballistic transport from a semi-classical understanding of electronic transport.

1.1.1 Diffusive Transport

In modern electronics, charge transport is diffusive. Charged carriers in an external electric field experience an electric force, which would naively result in continual acceleration. However, in a conducting material the carriers undergo scattering events after some average time interval t_m. Events such as these impede the carriers' motion and can be implemented in the equation of motion as a force term equal to $\frac{p}{t_m}$, where p is the carrier momentum [1]. The resulting Drude model assigns an effective mass (m^*) and Fermi velocity (v_F) to the carrier relating to the band structure of the material and defines the mean free path (L_m) to be the average distance between scattering events [2]:

$$L_m = v_F t_m. \tag{1}$$

Ohm's law, relating the voltage to the current flow across a channel, implies a constant resistance that can be explicitly defined using the Drude model. If we seek the steady state current density J where the electric force is balanced by the scattering to achieve a constant current, we find J to be a linear function of the electric field E [1]:

$$\boldsymbol{J} = \frac{ne^2 t_m}{m^*}\boldsymbol{E}, \tag{2}$$

where n is the carrier density and e is the electron charge. The linear coefficient is defined as the conductivity and its inverse as the resistivity. The mobility μ characterizes how freely the carriers respond to an external electric field and is defined as $\frac{et_m}{\mathrm{m}^*}$ [2]. Therefore, the resistivity ρ can be written succinctly as:

$$\rho = \frac{1}{ne\mu}. \tag{3}$$

Intrinsic quantities like ρ are independent of the quantity of the material of interest. Actual response of the total current (I) through a conducting channel, such as that shown in Figure 1, to an applied external voltage (V) requires consideration of the physical dimensions of the conductor. The extrinsic resistance R to the flow of current will be larger for a longer channel (length L). R will also be inversely proportional to the number of parallel channels, which increases linearly with the cross-sectional area A when there are a large number of channels.

$$R = \frac{V}{I} = \rho\frac{l}{A} = \frac{m^* v_F}{ne^2 L_m}\frac{L}{A}. \tag{4}$$

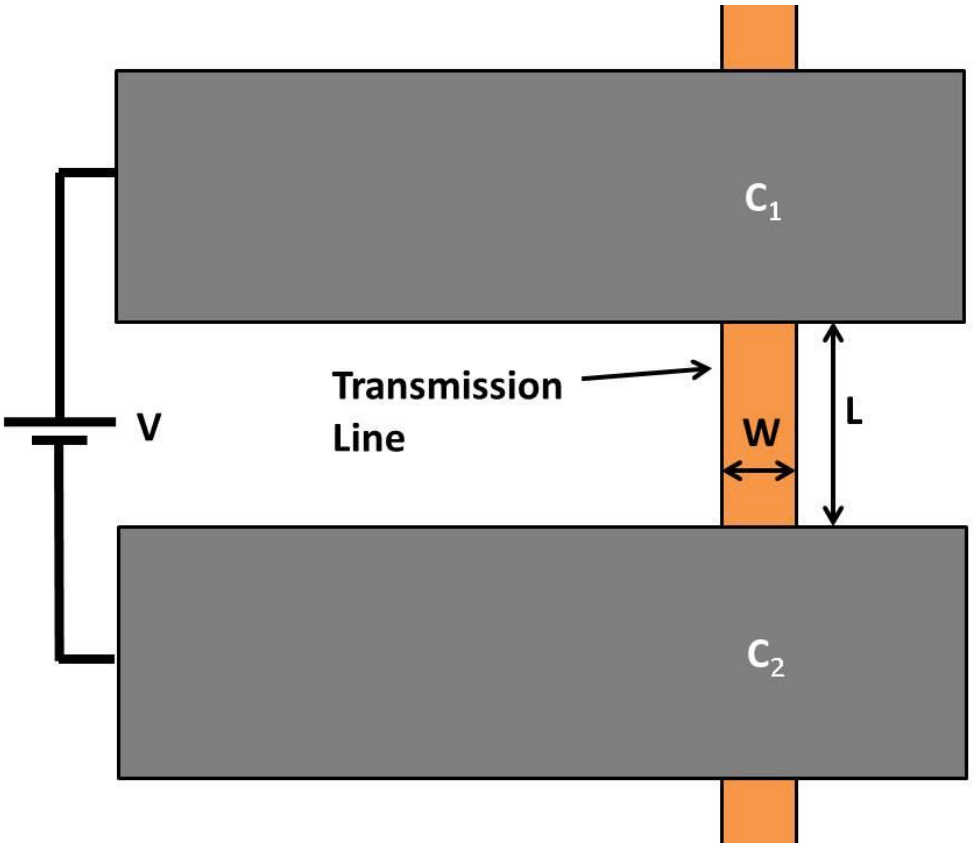

Figure 1 – Biased transmission line. Current flows through the transport channel in response to an external voltage applied across the contacts C_1 and C_2. The conductance is quantized in units of G_0 for each quantum channel in the transmission line.

1.1.2 Ballistic Conduction

For next generation electronics, nanoelectronics for example, the laws of quantum mechanics dominate. Quantum mechanics imposes an image of the electron as a coherent wave instead of a discrete particle that bounces off defects. As such, the wave vector k becomes an important variable in the electronic behavior of a material. The dispersion relation $E(k)$ reveals the band structure of a material and the Fermi-Dirac function describes how those bands are filled by carriers. In full quantum notation, an average extrinsic quantity is found by taking the product of the quantity of interest with

the Fermi-Dirac function and integrating across all of k-space. Scattering can then be seen as a loss of coherency and L_φ is a coherence length for the electron wavefunction. In high-mobility semiconductors $L_\varphi \sim L_m$ whereas in low-mobility semiconductors of polycrystalline films $L_\varphi \gg L_m$ [2].

Carriers in a narrow transmission line that is shorter than the mean free path of the material ($L < L_m$) will in general fail to be scattered and phase coherence is almost always guaranteed. This ballistic conduction results in a coherent wavefunction that stretches along and across the entire transmission line, quantizing in the lateral nano-scale dimension with a finite number of modes. Each mode contributes a discrete amount to the conductance of the channel, resulting in a model for ballistic conduction that invokes a maximum quantum conductance G_0 per mode. The recent International Technology Roadmap for Semiconductors [3] has recognized that when the channel length of field-effect transistors shrinks toward sub-10 nm length scales ballistic nanotransistors are required.

To derive the magnitude of G_0 we will employ the treatment used in Reference [2] which can be generally applied to any ballistic conductor independent of the dispersion relation. From Figure 1, $\mu_{1,2}$ stands for the chemical potential of contacts 1 and 2 and a difference between the two is responsible for current flow through the channel. We assume that current entering the wide contact from the channel is not reflected, such that all electrons moving toward C_2 come from C_1 and vice versa. The net current is the sum of these two electronic movements, where the forward current (I^+) moving toward C_2

and backward current (I^-) moving toward C_1 are given approximately by an integral over velocities and respective occupation probabilities [2]:

$$I^{\pm} = \frac{-e}{2\pi}\int v f^{\pm} dk = -\frac{e}{h}\mu_{1,2}. \tag{5}$$

The last equation here uses the quantum relation $v = \frac{1}{\hbar}\frac{dE}{dk}$ and the fact that the Fermi-Dirac function ($f^{\pm}$) at low temperatures is approximately a step function centered at $\mu_{1,2}$. The chemical potential is related to the electrical potential by the equation $-eV = \mu_1 - \mu_2$ such that the resulting I-V relationship is:

$$I = I^+ - I^- = \frac{-e}{h} * (-eV) = G_0 V. \tag{6}$$

This final result for the conductance assumes one non-degenerate ballistic channel and defines the quantum conductance $G_0 = \frac{e^2}{h}$. For a conductor with M channels each with imperfect transmission (T_n) the conductance is given by [2]:

$$G = \frac{1}{R} = gG_0 \sum_{n=1}^{M} T_n, \tag{7}$$

where g is any fundamental degeneracy like spin or valley degeneracies and M is an integer. Therefore, for any conductor composed of ballistic channels ($T_n = 1$), the conductance should be an integer M multiple of G_0 and be independent of channel length (as long as it remains shorter than the mean free path). The resistance of the ballistic conductor can then be expressed as

$$R = \frac{1}{gG_0M}. \quad (8)$$

1.2 Graphene Nanoribbon

Metal interconnects for semiconductor devices have gone through an evolution that mainly focused on fabrication possibilities and transport characteristics such as resistivity. Graphene, as a next-generation material recognized by the International Technology Roadmap for Semiconductors [3], allows for nanofabrication and quantum transport that make it far superior to classical metal interconnects. Because graphene is a naturally two-dimensional (2-D) material, narrowly confining the sheet into a nano-scale ribbon makes for an advanced interconnect for integrated devices.

1.2.1 Crystal Structure

Graphene nanoribbon (GNR) is a single atomic layer of graphitic carbon in the shape of a long thin ribbon. The carbon is arranged in a honeycomb lattice, as in Figure 2, with lateral confinement significantly less than one micron. This geometric structure is inherently ideal for compact one-dimensional quantum transport because of its diminutive sizes perpendicular to the direction of transport. Predictions of ever finer electrical devices [4] that are approaching critical limits with standard silicon and metal components can easily find room to expand through the use of GNR.

The sp^2 hybridized bonds between carbon atoms in graphene unite the hexagonal lattice in-plane, but leave an unhybridized floating pi bond that participates in conduction [5]. The primitive unit cell of graphene includes a basis of two carbon atoms that belong

to separate sublattices. The "pseudo-spins" of the floating pi bonds on these two sublattices tend to align antiferromagnetically and back-scattering of carriers between the sublattices is energetically disallowed.

The flavor of pseudo-spin becomes important at the edge of GNR. GNR edge termination is usually identified as some combination of two chiral possibilities: zigzag, where all the atoms on the edge reside on the same sublattice, and armchair, where the edge atoms alternate between sublattices, shown in Figure 2. When the width of the ribbon is on the order of or thinner than the extent of the pi bonds on the edges, the wavefunctions on the two edges begin to overlap across the ribbon and influence the electronic properties of the ribbon [5]. As such, the two edge configurations result in

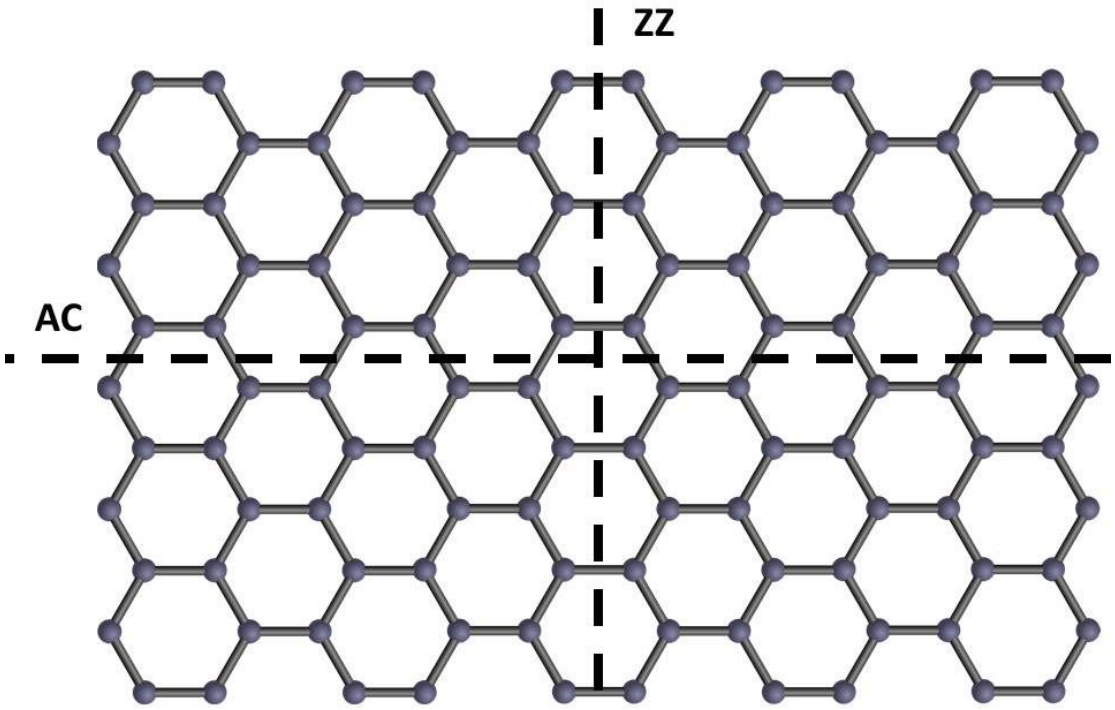

Figure 2 – Chiral edges result in two distinct ribbon types: Zigzag (ZZ) and Armchair (AC). The electronic band structure near charge neutrality will be very different depending on which chirality the GNR's edges are.

distinctly different electrical properties for transport down the length of the GNR, even to the point where an armchair ribbon can be insulating while the zigzag ribbon is conducting [6].

1.2.2 Band Structure

A nearest-neighbor tight bonding calculation for the band structure of an infinite 2-D graphene lattice reveals a zero-gap semiconductor with Dirac cones at the K (or K') point of the Brillouin zone that obey a linear dispersion relationship with a band velocity (c^*) of 10^6 m/s [7]. For intrinsic graphene (undoped), the Fermi level rests precisely at the Dirac point where the conduction and valence band touch. When one-dimensional confinement is taken into consideration, the band structure is adjusted to one with quantized subbands at energies related to the width of the ribbon [6]. The ability to distinguish amongst these subbands at finite temperature is determined by comparing the spacing of the energy steps to the thermal energy [8] in the approximation that the channel length L is $\gg$ than the channel width W. With ħ as the reduced Plank's constant and n as a positive integer then the energy of the nth is

$$E_n = \pm \hbar c^* \frac{n\pi}{W}. \tag{9}$$

Armchair and zigzag chiralities deviate on the band structure near the charge-neutrality point. An armchair ribbon can develop a bandgap or remain a Dirac cone depending on whether the edges are inverse in sublattice orientation or mirrored. A zigzag ribbon, on the other hand, hosts an edge state that is metallic at the Fermi energy at all low values of the width. The edge state has flat bands at $\frac{2}{3}\frac{\pi}{a} < |k| < \frac{\pi}{a}$ that is at the

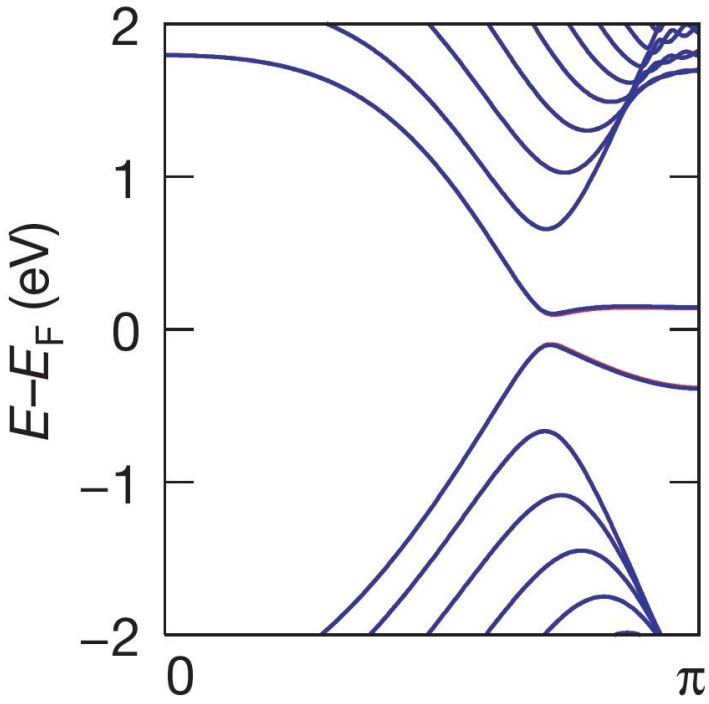

Figure 3 – Zigzag GNR band structure. The spin degree of freedom opens a band gap at $k = \pi$. The band gap at $k = \frac{2\pi}{3}$ is width dependent. Image courtesy of [9].

intersection of the conduction and valence bands and appears in all GNR with at least four zigzag sites in sequence [6]. When the edge state interactions are considered, it is found that the states interact anti-ferromagnetically as they are on opposite sublattices, causing a direct band gap and an energy splitting between the conduction and valence band [5], shown in Figure 3. A transverse electric field applied to such a ribbon will break the spin degeneracy and result in a widened gap for one spin state and a closed gap for the other, or what is called a 'half-metal' [9].

1.3 Epitaxial Sidewall Ribbon

The quality of experimental GNR depends heavily on the fabrication mechanism. A very narrow strip of graphene can be produced using nanolithography and plasma

etching, however the edge quality of such devices tends to be compromised by the aggressive process of plasma exposure and results in a series of quantum dots rather than a continuous edge state [10-12]. The theoretical description of GNR relies on an ordered edge state, so a means of producing crystallographic ribbon edges via a confined growth process would be ideal. Ribbon grown under such conditions should host a coherent edge state capable of all the properties explored in Section 1.2.

1.3.1 Growth

The growth of epitaxial graphene is a well understood process [13]. When silicon carbide (SiC) is heated to temperatures of around 1550 ℃ and the silicon vapor pressure is controlled, evaporation of silicon from the surface leaves behind carbon that forms into a graphene sheet. This 2-D crystal of well-ordered graphene on a semi-insulating substrate allows for a myriad of possible devices, especially when one considers the potential for patterned growth. With a hard, transparent, semi-insulating surface that has the potential to be shaped and grown into native and integrated graphene devices, SiC is a powerful platform for future electronics [14,15].

Self-organized growth on the $< 0001 >$ silicon surface [16] formed conducting channels of graphene on the naturally occurring steps edges preferentially over the flat SiC surface. The formation of GNR on a step edge presents the opportunity for patterned sidewall growth using plasma etched trenches to form fully customizable GNR devices and contacts [17]. Detailed characterization of sidewall GNR reveals a rich graphene structure with an extended ribbon across the length of the faceted step [18,19]. The facet angle produced by the heating of SiC is ~27° [8,20] so plasma etching and annealing

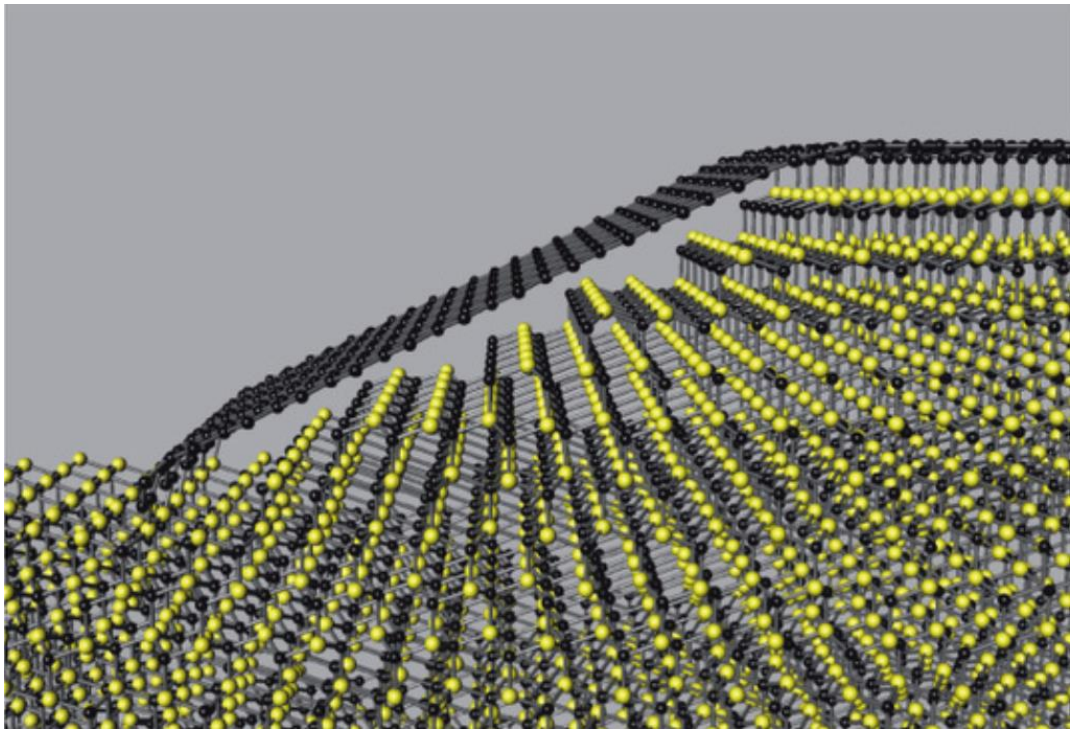

Figure 4 – Sidewall epitaxial graphene nanoribbon, an artistic rendition. The ribbon is expected to bond directly to the SiC lattice on the bottom edge and blend into buffer layer on the top edge. The complex geometry allows for a diverse set of potential theoretical explanations for the observed transport phenomena. Image courtesy of [8].

allows one to target specific ribbon widths by controlling the height of the sidewall on a nanoscale. The crystal direction of the sidewall with respect to the substrate has been shown to provide two distinct ways that epitaxial graphene nanoribbon (epiGNR) can be grown. Angle resolved photoemission spectroscopy performed on a variety of growth directions reveals that if the sidewall is perpendicular to the $< 11\bar{2}0 >$ direction of the SiC crystal lattice, growth primarily occurs on the tops of the trenches rather than on the sidewall itself [21]. If the sidewall is instead perpendicular to the $< \bar{1}100 >$ direction, the graphene ribbon is almost entirely isolated to the sidewall itself. This growth orientation is what will be referred to as epiGNR for the purposes of this dissertation.

Scanning tunneling microscopy and Angle resolved photoemission spectroscopy of epiGNR portrayed a graphene lattice with Dirac cones from continuous graphene coverage on the sidewall. The graphene is anchored at the bottom of the sidewall and merges into what is called the 'buffer layer' at the top of the trench [8,21,22], as illustrated in Figure 4. Buffer layer is a covalently bonded carbon layer that has a very similar crystal structure to graphene but has been shown to have a gapped band structure, even without in-plane confinement [13,22,23]. The conducting channel is thereby confined crystallographically to the sidewall by the surrounding insulating buffer layer and annealed SiC. Though the geometry of the system is complex, including an out of plane tilt to the 2-D graphene lattice, epiGNR is a generally stable structure that can be electrically accessed using standard fabrication techniques.

It is worth mentioning that commercial SiC wafers are cut using a laser with a small miscut angle of a fraction of a degree. The resulting surface has tiny, atoms-tall steps that are oriented in parallel across the entire wafer. During growth, these steps will flow and gather to form nanometer sized natural step edges across the surface that will then graphitize. These unintentional nanoribbons are unavoidable and must be considered during the fabrication process of an epiGNR device.

1.3.2 Properties

The physical properties of epiGNR inherit many of graphene's properties, which have become an exciting subject of research since the turn of the century [24-28]. Graphene is a fundamentally thin material as a stable, single-atom thick layer. Such structure gives rise to an extremely high surface to volume ratio and an astronomical

strength given how lightweight it is. Graphene absorbs 2.3% of white light [29], a very large fraction considering that it is only one atom thick. The electronic properties are also very interesting, starting from massless Dirac fermions that carry electrical signals at an exceptional speed. These carriers obey a linear dispersion relation as well as being immune to back-scattering. Other exotic properties include a fractional quantum hall effect [30,31], completely accessible atomic structure for chemical reactions [32], flexible physical structure [28], and an unusual van der Waals force [33]. However, the most important property of graphene for the purposes of this dissertation is its high carrier mobility [8,26,28,34-36]. Graphene has been shown to have a mobility far exceeding conventional conductors such as copper or gold, making it an ideal material for future transport applications.

1.3.2.1 Transport Properties

EpiGNR has a mean free path that is much longer than other conductors, allowing for practical experimentation of ballistic transport [8]. When simple length-dependent conduction measurements are performed, epiGNR indeed shows a non-linear length dependence that holds quantized conductance values below ~10 microns, as in Figure 5. In device lengths between ~1-10 microns, the ballistic conductance is a single quantum, pointing to single-channel transport in the ribbon [8]. This is an interesting result because graphene normally has a double degeneracy between spin and valley which should result in a conductance of $4G_0$ [27]. While lifting of the valley degeneracy is expected due to the lateral confinement, the lifting of the spin degeneracy is something of an anomaly. This single channel transport is temperature independent in pristine epiGNR [8] and, like 2-D graphene, exhibits a remarkably high mobility.

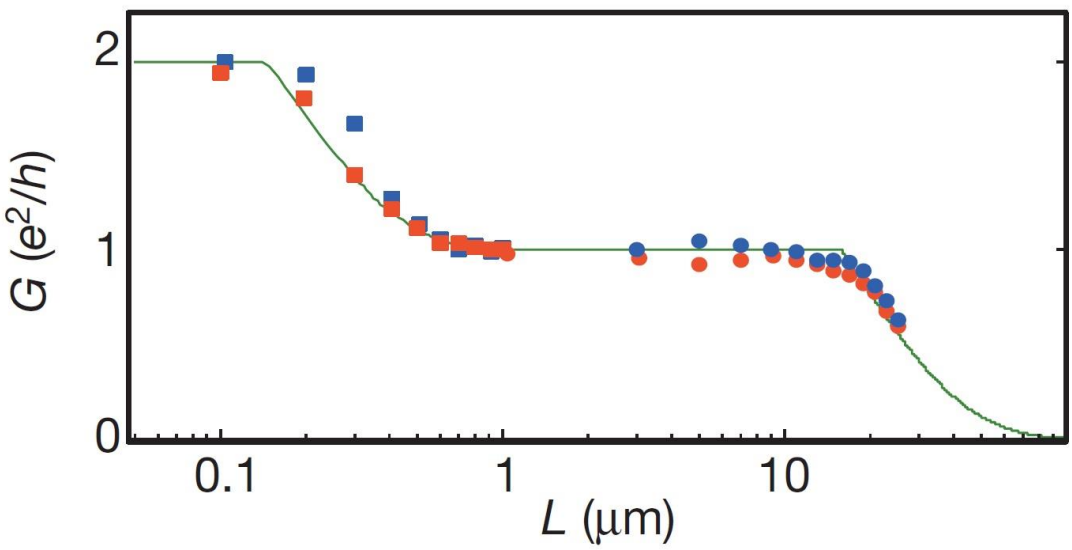

Figure 5 – Length dependence of epiGNR conductance. Single channel ballistic transport exists in the 1-10 micron length scale within epiGNR. In this range, the conductance is G_0 and length-independent. Image courtesy of [8].

1.3.2.2 Magnetic Behavior

Single channel transport ($g = 1$ in Eq. (7)) can only occur if the spin degeneracy of the channel is lifted. This is indicative of magnetic behavior, or some other interesting phenomenon that leads to a symmetry-broken ground state. To further probe the potential magnetic nature of the ribbon, ferromagnetic contacts were deposited on sidewall epiGNR [37,38]. Magnetic tunnel junctions fabricated with a cobalt (Co) ferromagnet and an aluminum oxide (Al_2O_3) tunnel barrier are sensitive to the spin polarization of the ribbon. Measuring the tunnel magnetoresistance through the Co-Al_2O_3-epiGNR interface presents a switching behavior [39] as the Co contact flips from a spin-polarized state that is parallel with the magnetism in the epiGNR to a state that is antiparallel. The relative magnitude of the measured change in resistance, as in Figure 6, depends on the spin polarization in both Co and epiGNR. This quantity is defined

through the density of the majority ($n_{\uparrow}$) and minority ($n_{\downarrow}$) polarized carriers and its value in Co is known [37]

$$Spin\ Polarization = \frac{n_{\uparrow} - n_{\downarrow}}{n_{\uparrow} + n_{\downarrow}}\ \%. \tag{10}$$

The spin polarization in sidewall epiGNR measured in this way has been shown to be as high as 78% [39]. The switch in tunnel magnetoresistance is also robust, surviving at temperatures up to 50 K and remaining in an anti-parallel state in magnetic fields as high as 14 T. The magnitude of the switch was also shown to be dependent on the angle between the magnetic field vector and the normal to the epiGNR surface [39].

The possibility of a ferromagnetic single channel graphene nanoribbon is of great interest in the spintronics community. Magnetic tunnel junctions themselves have been recognized as one of the most promising candidates for magnetoresistive random access memory which would allow for non-volatile, efficient, and high-speed computing [40]. Magnetic memory devices on epiGNR have the potential for extreme miniaturization and integration with other exotic and high-quality graphene components directly on the SiC substrate.

Spin and charge transport measurements like those performed in this dissertation provide a deeper understanding of the single-channel transport observed in sidewall epiGNR. Anticipation of a ferromagnetic ground state near charge neutrality is the motivation behind much of the work in this dissertation, however the nanoribbon as a high-quality interconnect is also explored. EpiGNR is an exciting next generation material and its exotic physical properties allow for a wide array of device applications.

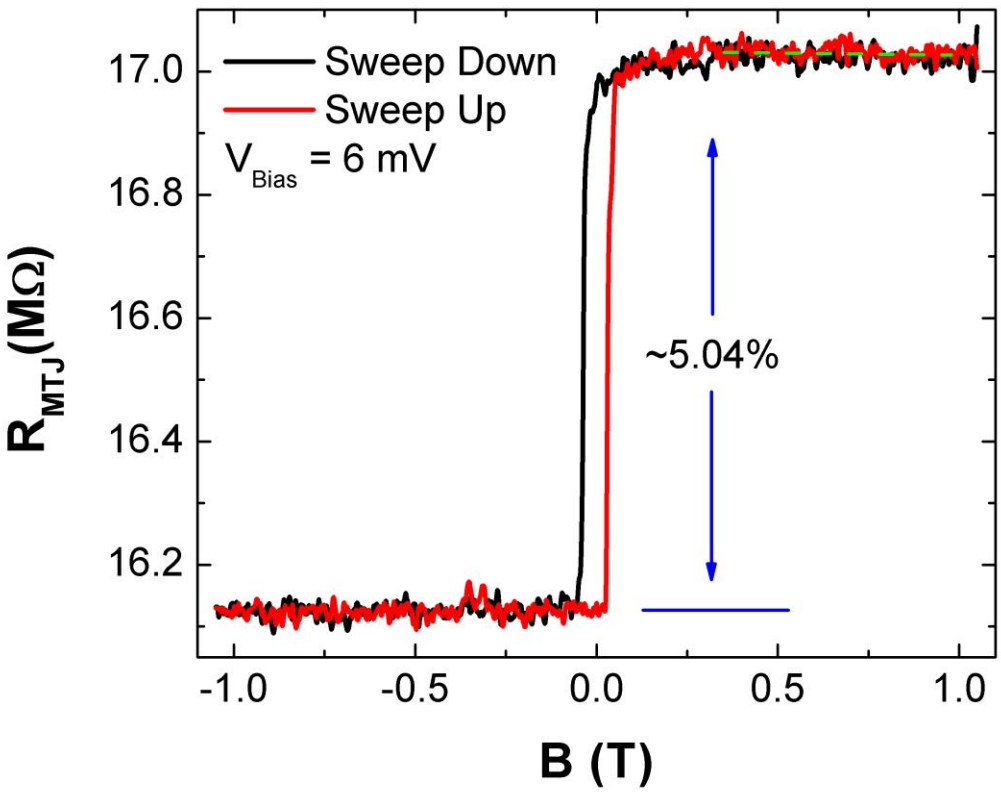

Figure 6 – Co-Al_2O_3-epiGNR Magnetic Tunnel Junction. A DC bias of 8 mV was found to produce the shown resistance switch between parallel (low resistance) and anti-parallel (high resistance) spin alignments. The width of the hysteresis loop is related to the width of the Co contact.

1.4 Dissertation Outline

Chapter 2 contains information about epiGNR device fabrication. Plasma etching and lithography are explored in depth as tools for circuit design. I present practical device geometries and patterns that were employed in the following chapters. Metallization techniques, specifically electron beam deposition, are discussed along with particular material choices for contacts and gates. Finally, I outline how the samples are mounted and measured at low temperatures.

Chapter 3 presents a superconducting proximity effect measurement on epiGNR. A brief overview of superconducting physics is given, culminating in a physical model for the superconductor-epiGNR interface. I explain the cryogenic 4-point measurement that was performed and highlight some of the challenges of a low temperature experiment. The conductance of the superconductor-epiGNR interface is measured as a function of magnetic field and bias voltage. The extracted zero-field spectra are compared with that expected from the theoretical model.

Chapter 4 describes a gate-dependent measurement of the electrical noise in epiGNR field-effect-transistor-like devices. I provide a theoretical background for understanding the low frequency noise and outline efforts to expose an extrinsic noise amplitude for comparisons between devices. By sweeping the carrier density in the ribbon, several aspects of the epiGNR channel are quantified, such as the doping level, mobility, and impurity density. I describe the observed ‘M’ shape of the noise amplitude and compare the quantitative noise characteristics of epiGNR with other carbon-based material systems.

CHAPTER 2. FABRICATION

2.1 Electron Beam Lithography

Lithography is the process of treating a substrate selectively to create a customizable pattern of material on the surface [41]. For many fabrication applications, the treatment is a polymer spin coating followed by electron beam or light exposure and chemical developing process. The resulting polymer structure can be used simply as a barrier to protect the surface from etching processes, or it can be used as a dissolvable separation layer for metal deposition. In the latter process, the edge of the structure is given an under-cut wherein the polymer closer to the substrate is developed wider than the top surface. This way, during isotropic deposition the metal landing on top of the polymer is entirely separated from the metal that will be left on the substrate, as in Figure 7. A proper liftoff will dissolve all of the polymer and take the extraneous metal with it, leaving behind a finely patterned circuit. This section records detailed information of the lithography process used in patterning epiGNR devices for transport measurements.

2.1.1 Polymers

The two biggest competing factors when choosing a polymer to use for lithography are the cleanliness and the ability to successfully liftoff large metal layers (or resist plasma exposure). Keeping the sample clean is extremely important for reproducibility and purity of the experimental results. As lithography requires the entire surface to be coated in polymer resist, we are limited to choices that are easily washed

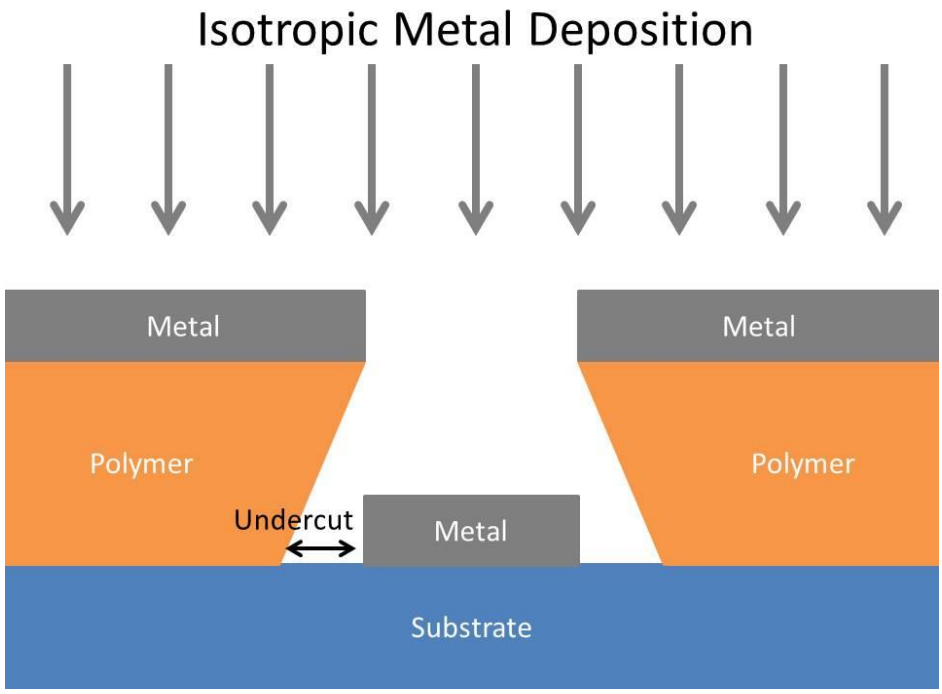

Figure 7 – Metal Deposition Using Lithography. The polymer provides liftoff to remove extraneous metals and leave behind only the desired circuit pattern. A wide undercut and a thick polymer layer give more liftoff power for thicker depositions.

away in solvent. 6% polymethyl methacrylate in anisole with 950,000 molecular weight (A6 950 PMMA) with methyl isobutyl ketone for developer has been found to dissolve in acetone with little remaining residue, or acetic acid for even cleaner polymer removal [42]. For this reason, it was used for a majority of the work presented here.

To improve the undercut and get better liftoff, a bilayer of resists can be used [43]. The lower layer should have a higher sensitivity to exposure so as to dramatize the profile and provide deeper exposure into the lower layer. Using a lower molecular weight (495 PMMA) or simply a lighter polymer (MMA), such a profile is achieved at a cost: these lighter molecules leave behind more residue on the graphene surface. As these polymers are more difficult to remove, a single polymer layer of 950 PMMA has

been the preferred method. Table 1 summarizes the spin recipes of the polymers used in this dissertation.

Table 1 – Polymer Spin Recipes. Electron beam and photo resists are included. *NR9-1500PY requires a post-exposure bake step of 100 °C for 60s.

Polymer	Speed (RPM)	Acceleration Rate (RPM/s)	Spin Time (s)	Temperature (°C)	Bake Time (s)
A6 950 PMMA	4000	500	40	180	90
A6 495 PMMA	4000	500	40	180	90
MMA	4000	500	40	150	90
Ma-N 2403	3000	500	60	90	90
E-spacer	4000	2000	60	N/A	N/A
HSQ	4000	2000	60	80	240
SC1813	5000	500	40	115	300
NR9-1500PY	4000	500	40	150*	60
HMDS	3000	1000	30	110	300
SPR220	1000	250	40	110	300

Developing a pattern involves submerging the exposed sample in a chemical solution for a short period of time. The active developing chemical is often diluted with water or isopropyl alcohol (IPA) to aid with uniformity and reproducibility. Underdevelopment will leave behind residue or an unwanted layer of polymer in the exposed regions while overdevelopment will weaken the edge profile by corroding

unexposed polymer. Agitating the sample by hand while in the development bath will ensure all areas of the pattern are evenly exposed. The sample is doused in water or IPA after the appropriate development time has passed to promptly cease the chemical process.

Some device designs can become very time consuming to expose using an electron beam. These designs can sometimes benefit from using a negative tone resist like ma-N, instead of positive like PMMA, such that the exposed part of the pattern remains while the unexposed part is washed away in the developer. Photolithography, on the other hand, can pattern large areas very rapidly by flooding the entire pattern at once instead of rastering. It uses many of the same principles explored in this section, though light-sensitive polymers are used instead of the electron-beam resists mentioned and the resolution is unfortunately limited due to physical constraints on the accessible wavelengths of light.

2.1.2 Beam and Dosage

A scanning electron microscope (SEM, JEOL 5910) equipped with a beam blanker and a nanometer pattern generation system (NPGS) is used to perform electron beam lithography. The electron beam is formed by heating a tungsten filament, drawing off electrons using a high voltage (30 kV), and collimating the beam using magnets. The beam is then rastered across the surface, exposing each section of the pattern in succession. The polymer absorbs energetic electrons and is chemically altered to respond differently to the developer compared to the unexposed polymer [41]. The conductivity and dielectric constant of the underlying substrate and its surface layer affect the local

dynamics of the beam and therefore the dosage requirements. For this reason, doing an experimental dose test to find the right dosage for the given substrate and application can save a lot of time wasted in mispatterning.

There are many strategies to improve the quality of one's lithography. Errors in writing can be minimized by finely focusing the beam on the substrate surface and wisely choosing the raster direction for a given object. To minimize line width, consideration of the physical effect of the electron beam on the polymer is prudent. Beam exposure will either disrupt the polymer chains for a positive tone or cause cross-linking amongst them in a negative resist. Some polymers, like PMMA, have both effects and, even though one dominates over the other, an overexposure can result in a poorly defined polymer edge profile. For this reason, there is a certain ideal dosage that is dependent on the quantity and type of polymer on the surface. The spin time and speed as well as the bake time and temperature form a recipe for attaining a smooth layer of resist of a particular target thickness. On the other hand, development is a saturation process that is done until completion so the time required is only weakly dependent on the recipe thickness. The dosage (D) in units of energy per area represents the magnitude of exposure to the beam, which will cause the desired chemical change in the polymer upon exceeding the threshold value. The rastering of the beam is done in discrete movements, with each movement having a dwell time given by:

$$T_{Dwell} = \frac{D}{I_{Beam}}(L * W). \tag{11}$$

Here, the beam current (I_{Beam}) is calibrated before each run, while the line spacing (L) and center-to-center distance (W) of the electron beam spots are controlled by the NPGS program. The total time per unit area required for exposure is given by $\frac{D}{I_{Beam}}$ so increasing the rate of electrons incident on the polymer gives a straightforward way to decrease the patterning time. However, the beam of negative particles will interfere with itself and a high current can cause divergence that will produce a weak polymer edge profile, thereby limiting the resolution of the beam at high currents. To produce a well-defined pattern with high resolution, the lithography recipe is restricted by a minimum T_{Dwell}. Because the electron beam must dwell on each part of the pattern in succession, electron beam lithography is considered a time intensive process without potential to scale up.

In industrial and large scale production applications photolithography is often used due to its ability to parallel process the exposure step using an optical flood. In such procedures, a fused silica mask is manufactured with each lithographic step of the process written side by side. Alignment between the steps becomes crucial and complementary alignment marks are placed surrounding each pattern. These masks are rigid, somewhat expensive to create, and cannot be changed. Electron beam lithography, on the other hand, allows for a much more precise control over the pattern on the order of 10 nm (as opposed to photolithography's micron resolution) and the pattern can be programmed into beam movement on the fly using NPGS and Design-CAD. Though electron beam lithography is not ideal for large throughput, its fine line width and flexibility makes it very useful for the prototyping done in this dissertation. Example polymer dosages and developing recipes are shown in Table 2.

Table 2 – Polymer dosages and developer recipes for positive (P) and negative (N) resists.
***Magnification and pattern specifics, such as desired resolution, will affect the ideal dosage. Dosage tests are done often to recalibrate.**

Polymer	Type	Dosage*	Developer	Develop Time (s)	Wash
A6 950 PMMA	Ebeam (P)	250-400 $\mu C/cm^2$	3:1 MIBK:IPA	20	IPA
A6 495 PMMA	Ebeam (P)	250-400 $\mu C/cm^2$	3:1 MIBK:IPA	20	IPA
MMA	Ebeam (P)	250-400 $\mu C/cm^2$	3:1 MIBK:IPA	20	IPA
Ma-N 2403	Ebeam (N)	120 $\mu C/cm^2$	MF-319	30	DI water
HSQ	Ebeam (N)	1500 $\mu C/cm^2$	TMAH 25%	30	DI water
SC1813	Photo (P)	150 $mJ/cm^2/\mu m$	MF-319	20	DI water
NR9-1500PY	Photo (N)	190 $mJ/cm^2/\mu m$	3:1 RD6:H_2O	60	DI water
SPR220	Photo (P)	Laser Writer	MF-319	240	DI water

2.1.3 Device Patterning

The NPGS program allows a user to upload a design image made in Design-CAD directly for patterning with the SEM. To attain high resolution at small length scales, a high magnification (typically 1,000x) is used for the inner pattern. The outer pattern, on the other hand, requires large-scale pads for to wire bond and contact the inner pattern. Attempting to do large-scale patterning with high magnification results in extremely long write times and prohibitive field-stitching concerns. Writing the pattern at several different magnifications provides tunable resolution to different sections of the pattern such that the write speed can be optimized. The areas of the pattern that connect across

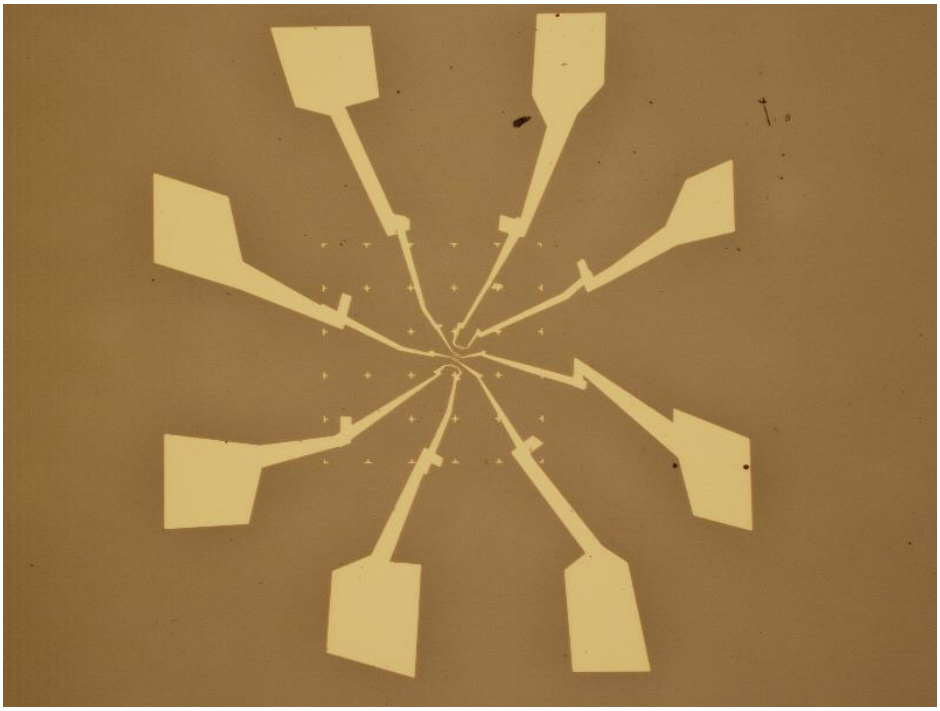

Figure 8 – An Epitaxial Graphene Nanoribbon Device after depositing metal contacts. To form both small contacts and large wirebonding pads, three different magnifications, 95x, 230x, and 1,000x, are used and hook-like features are made to increase the tolerance for shifts between magnifications. The grid of crosses is used for alignment to the nanoribbon at the center of the device.

different magnifications are designed to provide as much tolerance as practical for random shifts in the beam, resulting in the hook shapes seen in Figure 8. Systemic shifts occurring from magnification changes are well calibrated and written into the NPGS run file.

As epiGNR is not easily visible in an SEM, especially under a layer of polymer resist, alternative methods must be used to align the pattern with the ribbon. Alignment marks can be made directly on the polymer and developed as an additional lithography step prior to patterning. The relative location of the epiGNR with respect to the alignment marks can be imaged under an optical microscope and uploaded to the NPGS

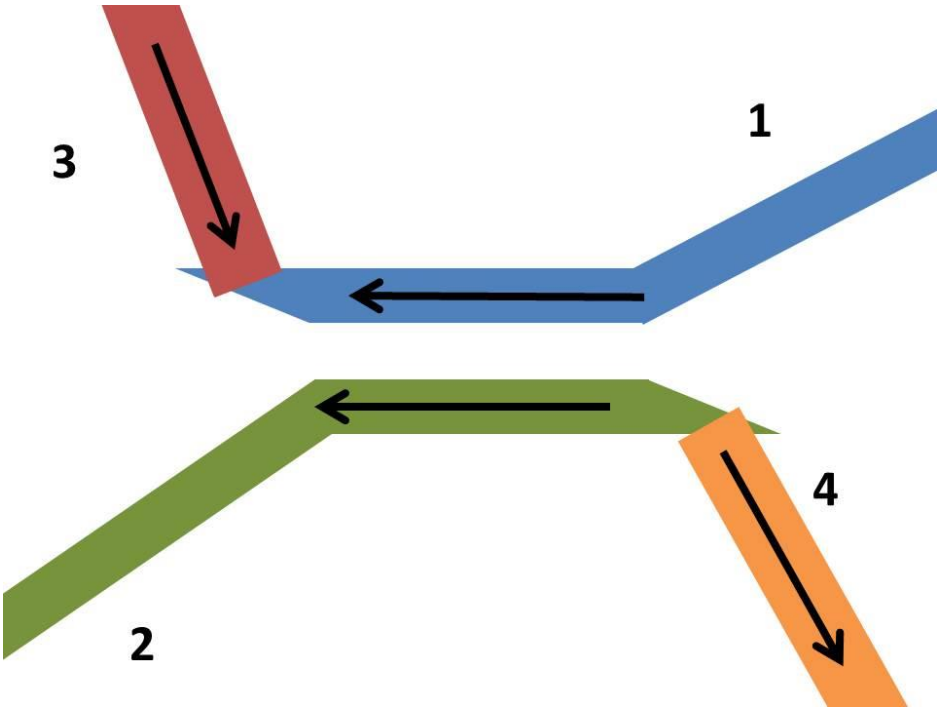

Figure 9 – Contact Schematic for making dual sided contacts with narrow spacing (≤1 μm). Arrows represent scan directions and the order of drawing the objects is numbered. The raster will only move a minimal distance between blue and green objects, thereby reducing contact spacing error.

computer for automated alignment. Alternatively, to reduce the number of steps or in case a positive resist is desired (negative resists cannot be developed more than once like positive resists can) permanent metal alignment marks can be deposited that can be seen by the SEM through the polymer.

Device geometries can vary widely and require many different techniques to problem solve. For certain ribbon measurements like superconducting proximity effect the contacts may need to be both double sided (having two terminals on one contact) and very narrowly spaced. These requirements make for a very crowded device geometry where fabrication risks an electrical short or poor lift-off. By focusing on the scan direction and intelligently designing the contacts to be drawn in two stages, like in Figure 9, the pattern can be exposed with as little movement as possible between objects and therefore reducing the chance for error.

2.2 Plasma Etching

Etching away the surface of a substrate is a powerful fabrication method for both crafting the geometry of the surface and removing unwanted materials. Reactive plasma is struck in a chamber filled with gas using a radio frequency electromagnetic field. This plasma both bombards and reacts with the sample surface, etching the surface via two distinct mechanisms. Reactive Ion Etching (RIE) uses a capacitive plate to increase the rate of bombardment for a more anisotropic etch and allows for fine control over the depth of the etch on the order of a nanometer for most materials. Inductively Coupled Plasma (ICP) includes an inductance coil, which generates a magnetic field that can be used to increase the plasma density and the rate of chemical reaction. While RIE etchers

were used for all lithographic etches in this dissertation, the plasma-therm ICP gave very anisotropic etches because it used both a capacitive plate and an inductance coil to finely control the density and kinetic energy of the plasma. This particular machine also had the ability to do the Bosch process, which is a specialized two-mode silicon etch that switches between a deep isotropic etch (using SF_6) and deposition of a passivation layer (C_4F_8) to enhance deep directionality of the etch. The ICP machine was therefore used for making masks out of silicon and very deep trench structures (>100 nm) while RIE etchers were used for the majority of sample preparation. Commonly used etch recipes are shown in Table 3.

Table 3 – Etch recipes. Etching graphene and 30 nm deep trenches encompassed the majority of the work in this dissertation. The BOSCH process was used to customize a Si shadow mask.

Material	Machine	Gas	Pressure (SCCM)	Time
Graphene	Samco RIE-1C	O_2	4	30s
SiC (30 nm)	Vision 2 RIE	O_2/Ar/SF_6	10/7/13	55s
SiC (150 nm)	Plasma Therm ICP	O_2/CF_4	5/15	60s
Si (through)	Plasma Therm ICP	BOSCH	--	1500 cycles

2.2.1 Sidewalls

For sidewall graphene growth, a locally defined trench needs to be etched in SiC. Fluorine ions in plasmas of gasses like CF_4 and SF_6 are known to etch the surface of SiC [44] with a reproducible rate. By etching along the $< \bar{1}100 >$ direction (known from the commercial wafer) the surface is well prepared for epiGNR growth. An atomic force microscope (AFM) can tap a hyperfine needle across the surface of the etched substrate, providing an image of the substrate post etch and pregrowth. Other than providing

verification of a smooth etch with smooth trench bottoms, these images can reveal the miscut direction of the manufactured SiC substrate.

There are many changes after the sample is put through the induction furnace. Steps in the SiC surface, both deep and shallow, will facet and flow during high-temperature annealing. Natural steps on the surface due to the miscut angle will gather and form into sidewalls a few nanometers tall [45]. These natural steps will merge with an etched sidewall, causing complicated surface geometries. Still, when the surface graphitizes at higher temperature the sidewalls grow continuous and high-quality epiGNR of controllable width and form. The bottoms of the trenches tend to have very poor growth compared to the buffer layer and natural steps on the polished SiC surface. As the trench bottom is insulating, however, exploration of that area is outside our scope of transport physics. Future devices seek to simplify the geometry by using the natural steps themselves as the desired sidewall rather than plasma-etching one into the substrate, however the work in this dissertation will use plasma etched trenches ~30 nm deep.

2.2.2 Ribbon Characterization

Epitaxial graphene is an extremely thin material with a known Raman absorption spectrum [46]. However, because epiGNR is much narrower than the spot size of standard micro-Raman spectroscopy equipment it is very difficult to determine the quality of graphene growth prior to device fabrication. Initially, the primary technique used for ribbon imaging was electronic force microscopy (EFM) which is an AFM mode that measures the static electric forces on the surface by driving the conducting cantilever (ppp-EFM) with an AC electric field. Because the conductivity of graphene is so

different from the surrounding SiC and buffer layer, EFM would give a good signal on well-grown epiGNR. However, if the tip is unable to respond quickly to a topographical change, the separation distance with the surface will change and a false EFM signal will be measured [39].

To eliminate false EFM signals, attempts were made to directly measure the change in work function as graphene has a work function that differs from bare SiC by ~0.7 eV [47]. Scanning kelvin probe microscopy uses an additional feedback loop to eliminate the effect of surface charge [48] and provides the work function image that we desire. This mode is more effective at distinguishing between well-grown ribbon and poorly grown ribbon than EFM, however it is still unreliable at times due to mixing of the topographical signal.

Further research into rapid GNR characterization led to a friction mapping using lateral force microscopy (LFM) [49]. This AFM mode uses a contact cantilever (SHOCONA) and measures the lateral distortion on both forward and backward sweeps, revealing the magnitude of the friction coefficient for different areas, even on the sidewall itself. The images produced by this method are extremely clear because of graphene's abnormally small friction coefficient, providing a useful characterization of the ribbon post-growth but before device fabrication.

LFM of the SiC surface on a properly grown sidewall epiGNR sample revealed the prevalence of natural step growth across the entire surface. These ribbons converge with the etched sidewalls, causing meandering edges and locally complex structures. With a pre-growth annealing process, these natural steps can be accentuated and the

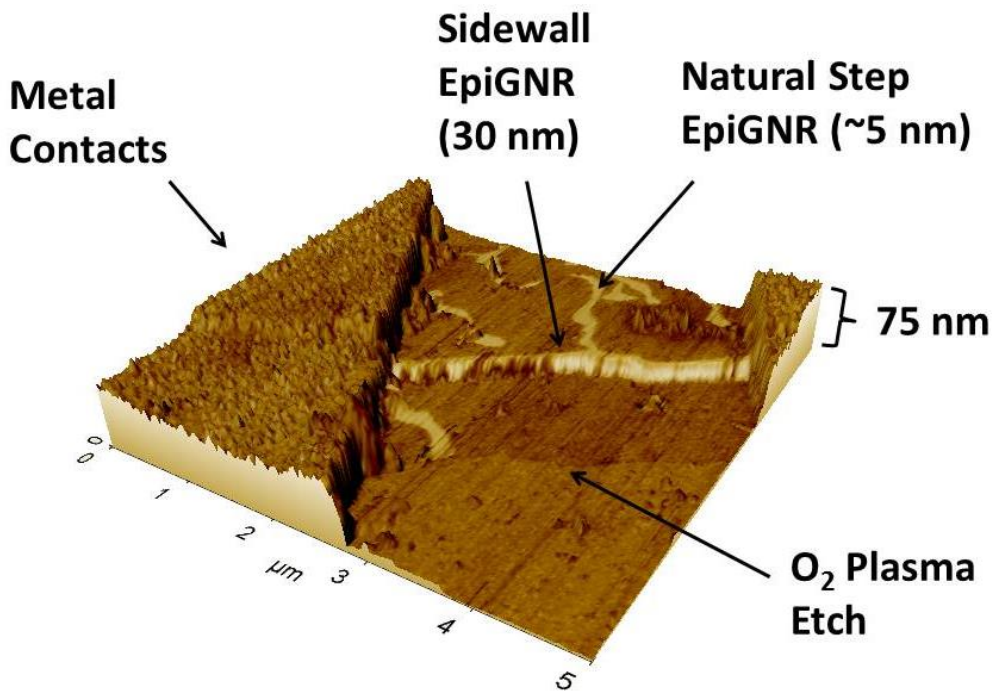

Figure 10 – LFM image mapped onto 3D topography of epiGNR junction. O_2 plasma severs meandering natural step ribbons while sidewall epiGNR is confined to the SF_6 etched edge. Metal contacts allow for direct transport measurement of the conducting channel.

ribbons they produce can be targeted for device fabrication. As steps that small are hard to see optically, they can be located relative to deposited metal alignment marks using LFM imaging. However, as the growth recipe for etched trench growth has been explored in-depth [16], this dissertation mostly relies upon structures of that nature. Future studies will likely focus on annealed miscut angle sidewalls rather than plasma etched structures.

2.2.3 Plasma Purging

Oxygen plasma readily reacts with graphene, allowing it to strip the device area surrounding the graphene channel of interest [50]. Lithography is used to protect the

targeted ribbon such that it is the sole conducting channel between pads and corresponding contacts. Devices formed in this way measure the ribbon directly and signals sent down its length probe its transport properties. The chosen contact material as well as the surrounding environment and geometry will reflect the intended experiment. Device materials used include normal metals, ferromagnets, superconductors, and dielectrics.

2.3 Metal Deposition

Polymer liftoff is a very powerful method of sample metallization because it provides a large freedom for pattern design and well defined pattern edges. To make the best use of the lithographic undercut, an isotropic deposition that will not coat the edge of the polymer pattern is preferred. A jet of metallic gas, such as that produced in electron beam evaporation, can provide the desired directionality [51]. Evaporation of a material like gold is readily done using an electron beam that arcs via magnetic field from a heated filament into the crucible holding the evaporation material, shown in Figure 11. Thermal evaporation by heating the material with a filament directly also results in gaseous metal, but some metals require the concentrated power of an electron beam to reach evaporation temperatures. Sputtering ejects a stream of particles using energetic particle bombardment on a metal target [52] and while this allows for a very broad set of potential deposition materials, it is not as isotropic as electron beam evaporation and the high energy particles ejected from the film can damage the thin monolayer of graphene. Atomic layer deposition is very efficient at producing thin films. However, the finite number of recipes for its two stage chemical process greatly limits the potential deposition materials, such that the method is only useful for Al_2O_3 deposition for gate

dielectrics. For these reasons, electron beam evaporation will be the primary method of metallization used in this dissertation.

2.3.1 Electron Beam Evaporation

The acceleration voltage that draws the electron beam from the filament is limited by what is safe and practical, so it is the power through the filament that is controlled to vary the deposition rate. As the beam spot is optically visible while heating the metal in the crucible, the vacuum chamber is equipped with a window for manual alignment. The metal glows as it is heated and begins evaporating in the local area where the electron

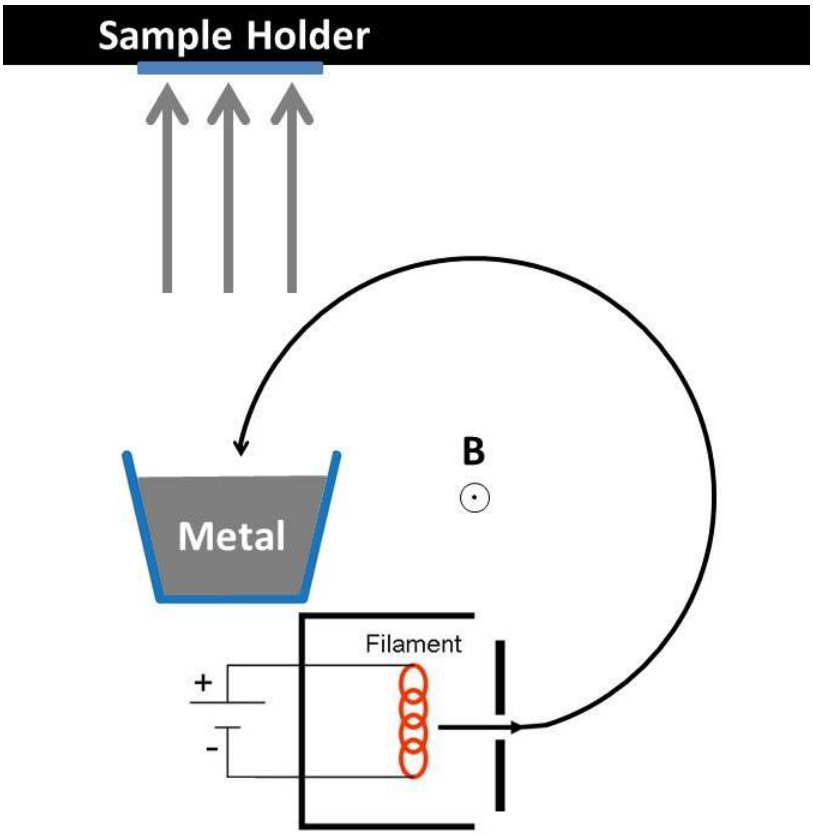

Figure 11 – Electron Beam Evaporator. The substrate is held upside down over the evaporation source and a magnetic field is used to bend the beam into the crucible.

beam is focused. The crucible must be able to withstand the heat of molten metal and so is most often a form of carbon (such as Fabmate), though special materials like boron nitride may be required for particular metals like Al with exceptionally high chemical activity at their evaporation temperature [53]. Crucible liners, which are essentially smaller crucibles that go inside the normal crucible, provide several benefits just a crucible alone. The liners allow for quick material changes and reduce heat transfer to the crucible. They minimize maintenance and lower cost of ownership because they are smaller and thinner than the crucible. Crucible liners are most often used when a material is particularly expensive, difficult to evaporate, or when cross-contamination is a large concern.

Gold (Au) is non-corrosive with good conductance, making it a useful capping material for a metallic contact. To form a transparent contact with graphene, a layer of palladium (Pd) should be used [54] as the coupling length of the graphene-Pd interface is shorter than the mean free path in the graphene channel [55]. Co can be used for a ferromagnetic contact, though a special crucible is required like with Al. For devices like spin valves, an insulating tunnel barrier can act as a spin filter to increase the injection polarization from the Co layer. A slow (0.2 Å/s) and extremely thin (~5 Å) Al deposition will rapidly oxidize to form the insulating barrier desired. A very fast (5 Å/s) and low pressure (10^{-6} Torr) deposition of high purity Al (≥99.999%), on the other hand, will result in an Al layer capable of superconductivity at low temperature (with a superconducting transition temperature ~1.2 K) [56]. In any case, mounting the sample on a rotostrate will help ensure full coverage of exposed areas and as little deposition on the polymer sidewall as possible, aiding with a clean lift-off.

2.3.2 Lift-off and Shadow Masks

A solvent like acetone will dissolve polymers during the lift-off stage and provide a separation force between the wanted and unwanted regions of deposited metal. Many industrial applications for lift-off include a sonication step where the acetone bath is subjected to ultrasonic vibrations to aid in separating the material in the exposed region from that resting on the dissolving polymer. However, graphene is known to separate from the surface upon sonication, especially epiGNR which has such a unique geometric structure, so all sonication should be avoided out of fear for damaging the sample. Heating the covered acetone bath to a temperature of 45°C is appropriate to aid the lift-off but avoid solvent evaporation. Most lift-offs were done overnight, though more rapid lift-offs have been done successfully in the past. When ready, the sample is lifted to the surface of the bath and a spray bottle is used to shoot acetone at an angle on the substrate so as to separate the metallic film from the substrate surface. After cleaning with isopropyl alcohol and blowing dry by compressed nitrogen gas, an optical microscope is used to inspect the sample. In some cases, where the lift-off fails and metal remains causing an electrical short between large pads, micromanipulators connected to sharp pins can be used to mechanically cut the electrical connection and isolate the contacts.

Some experiments require extremely clean samples and all chemical treatment is avoided after graphene growth. Metallization without lithography is a particularly interesting challenge, often approached by some attempt to block the metal evaporation jet with a solid object [57], as seen in Figure 12. These shadow masks can be made of many things, such as wire or mesh, that create very basic shapes on the surface such as large separated pads or islands respectively. For more direct control over the shape of the

deposition shadow a rigid silicon or silicon nitride mask can be selectively etched with lithography and the Bosch process, though etching entirely through a silicon wafer can be tedious and the resulting mask fragile. Kapton tape can also be used as a shadow mask and can be shaped with a lot of freedom, however it defeats the original purpose of avoiding chemical contact with the sample.

The boundaries between deposited and undeposited areas on a sample are very different for lift-off processes compared with shadow mask deposition. Because the mask is rigid there tends to be a small gap between the substrate and the mask that causes shadow depositions to appear fuzzy, having a vaguely defined boundary that can be on

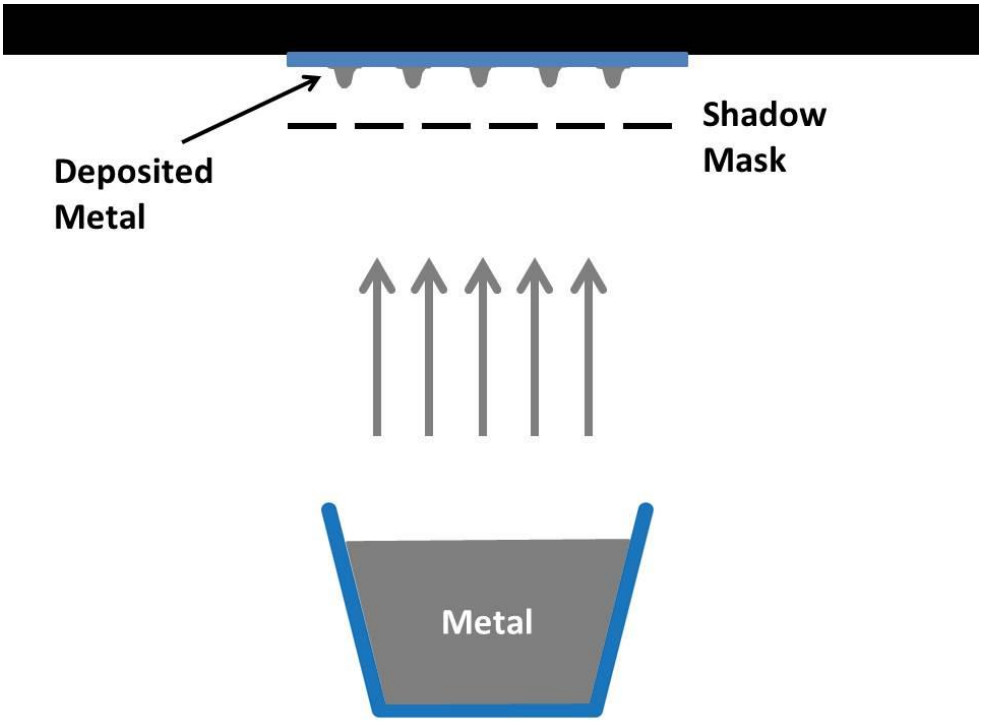

Figure 12 – Shadow Mask Evaporation. The stencil provides liftoff without using a polymer mask. As there is some separation between the mask and the sample, the resolution is lower for a shadow mask than polymer lithography.

the order of 1 μm wide depending on the specific construction of the shadow mask and the deposition thickness. Lithography, on the other hand, causes sharp edges that spike up from the lift-off process. Edges created by lift-off tend to be around a thousand times thinner than the taper of the shadow mask edges, making lithography preferred over shadow mask depositions for nano-patterning even when pattern restrictions due to mask fabrication are ignored.

2.3.3 Gate Dielectric

Direct control over the carrier density in the channel of a transistor-like device is achieved using a dielectric coating with a capacitive electrode. Al_2O_3 can be deposited as the insulating dielectric via a multi-step electron beam deposition of oxidized Al. The evaporation is done at a very slow rate (0.2 Å/s) and at as high a pressure as can be safely achieved (~10^{-5} Torr). A deposition of this sort will allow the Al atoms the best opportunity to find an oxygen atom in the chamber atmosphere and bond with it before landing on the substrate. The thin (~10 nm) film of Al is then removed from the vacuum chamber to allow for a complete passivation layer to form [58]. The sample is then rotated so as to ensure complete coverage and minimize shorts across the insulating film and the deposition is repeated. This is often repeated a total of 3 times for a 30 nm thick gate dielectric. The electrode is formed by a fast deposition of Al (1 Å/s) at low pressure (~10^{-6} Torr) capped with Au to prevent electrode oxidation. The metal stack produced in this way is very effective as a top gate for the graphene channel.

2.4 Measurement Preparation

2.4.1 Device Characterization

Transport devices fabricated using lithography are made with conducting pads on the substrate surface for electrical connection with the sample. An optical microscope allows for a cursory check that there are no obvious shorts or breaks, but electrical contact is necessary for full transport characterization of the device. A probe station uses needle leads connected to micromanipulators to push down on the pad and make good but temporary contact with the sample. More advanced probe stations can even put the sample chamber under vacuum and go to cryogenic temperatures. The ability to readjust or even move the leads between measurements is a big benefit for preliminary tests. However, the contact resistance due to effects such as oxidation of the tip make probe station measurements less reproducible and at times less insightful than other more permanent methods of creating sample leads. Combining the transport measurements of the probe station with a direct imaging method like AFM results in a powerful set of data to characterize the sample even before creating the final contact leads.

2.4.2 Mounting the Device for Measurement

The SiC chips used primarily were cut into 3.5 mm x 4.5 mm rectangles with one corner chipped to identify the silicon-terminated surface and miscut direction. Silver paste is used to secure the chip into a mounting stage with 16 pins, imaged in Figure 13. A wire bonder uses heat and pressure to attach 25 μm diameter Al wires from pin to sample. The sample is then ready to be plugged directly into a probe and measured. The probe is often connected to a break out box with individual BNC female connectors and a grounding switch for each pin. The probe is pumped down to low pressure (~10^{-5} Torr) and can be placed in a liquid nitrogen dewar for quick low temperature measurements (~77 K). Alternatively, a Helix CTI-Cryogenics closed-cycle refrigerator that uses a

compressor and a cold head can bring the sample down to ~10K rapidly. In either case, great caution and patience is needed when bringing the sample back to room temperature to avoid condensation of water particles on the sample surface. These techniques are useful for measuring samples quickly and with low cost, however most advanced measurements in this dissertation were done using a Janis ^{3}He system (0.3 K to 300 K and equipped with a 14 T magnet) as described in Section 3.2.2.

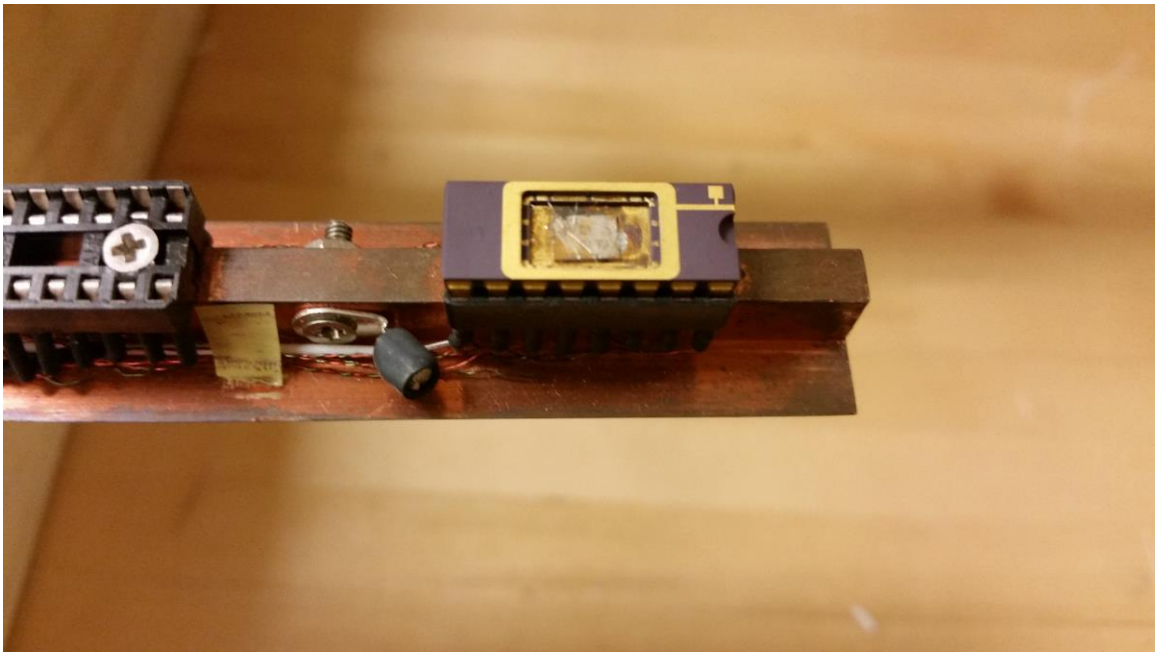

Figure 13 – Stage with Mounted Sample. 16 pins are connected to individual contact pads via wire bonding. This mounting stage is used for low temperature and low noise measurements.

CHAPTER 3. SUPERCONDUCTING PROXIMITY EFFECT

In addition to spin transport measurements on epiGNR carried out by Dr. Hankinson et al. [39], we seek to find other methods to address the magnetism in epiGNR. The superconducting proximity effect, when understood with a theory that accounts for ferromagnetism, provides information about the spin polarization of the material [59-64]. With an appropriate physical model for comparison, we measure the transport properties of epiGNR devices with superconducting contacts.

3.1 Introduction to Superconducting Proximity Effect

In some materials, lattice vibrations, or phonons, have an attractive effect on electrons at low temperatures. Below a critical temperature (T_C), the phonon induced attraction will overcome the Coulombic repulsion and form coherent pairs of electrons described by a wavefunction that obeys a set of principles according to Bardeen-Cooper-Schrieffer (BCS) theory [65] and the London equations [66]. Consequently, a superconducting energy gap (Δ_{SC}) in the density of normal electronic states forms at the Fermi energy. In place of normal electronic carriers, the transport signal is carried by pseudo-particles that experience infinite conductance up to a critical current (I_C) at which the material turns normal again.

Many common materials are superconductors at low temperature, such as Al, niobium, and lead, making nanofabrication of superconducting devices a viable experimental field. There are also other more exotic superconductors, all with different T_C. One particular group of superconductors that show large promise of having an especially high T_C is cuprates, compounds that contain copper-oxide (CuO_2). The *d*-

orbital states in a Cu^{2+} ion combined with the perovskite structure of cuprates are responsible for their high T_C [67]. However, while more exotic superconductors are attractive, such materials are not easily formed into metallic contacts for an epiGNR device. Al is a common evaporable metal with an accessible $T_C \approx 1.2$ K and *s*-wave superconductivity that can be fully described by BCS theory. As such, evaporated Al contacts make a prime candidate for the study of the superconducting proximity effect in epiGNR.

In a type I superconductor below $T_{C,}$ electrons or holes will couple together into Cooper pairs of opposite spin and create spin-0 (*s*-wave) bosons, so as to minimize the electron-electron interaction energy including the exchange energy [65]. The Cooper pairs obey Bose-Einstein statistics, and so condense into a ground state by undergoing a phase transition, resulting in a gapped density of states with sharp occupation peaks (van Hove singularities [1]) at the gap energy. In the bosonic ground state the electron wavefunction manifests as supercurrent which undergoes no resistance when traversing the superconductor [68]. The superconducting transition in a uniform Al channel will therefore go from a normal state of finite resistance to a zero resistance superconducting state.

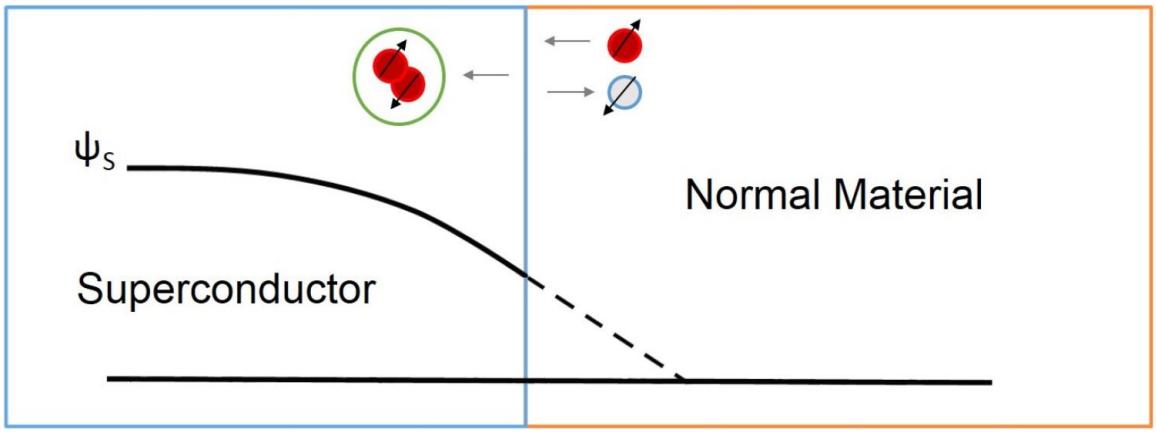

Figure 14 – Interface between a superconductor and a normal metal. In the normal metal the electron and hole pair maintain coherence within short proximity due to Andreev reflection. In the superconductor the energy gap near the interface is reduced due to the presence of normal material (no gap)

3.1.1 Superconducting Proximity Effect

At the interface between a superconductor and a normal metal (SC/NM interface), the electron wavefunction will maintain coherence for some distance into the normal material, resulting in the superconducting proximity effect (see Figure 14). The microscopic mechanism of this effect is described by the so called Andreev reflection process in which an incident electron with energy $E < \Delta_{SC}$ gets reflected back as a coherent hole of opposite spin [69] with a coherency energy that is analogous to the Thouless energy in a mesoscopic system [70]. At such an interface, two charges pass into the superconductor for each incoming electron so the conductivity is doubled compared to a normal metal-metal interface. This proximity effect also reduces the superconducting gap energy of the bulk superconductor near the interface (see Figure 14), which can be modeled as a thin superconducting film with a second gap energy Δ_{RPE} lower than that of the parent Δ_{SC}. This effect is usually referred to as the reverse proximity effect (RPE).

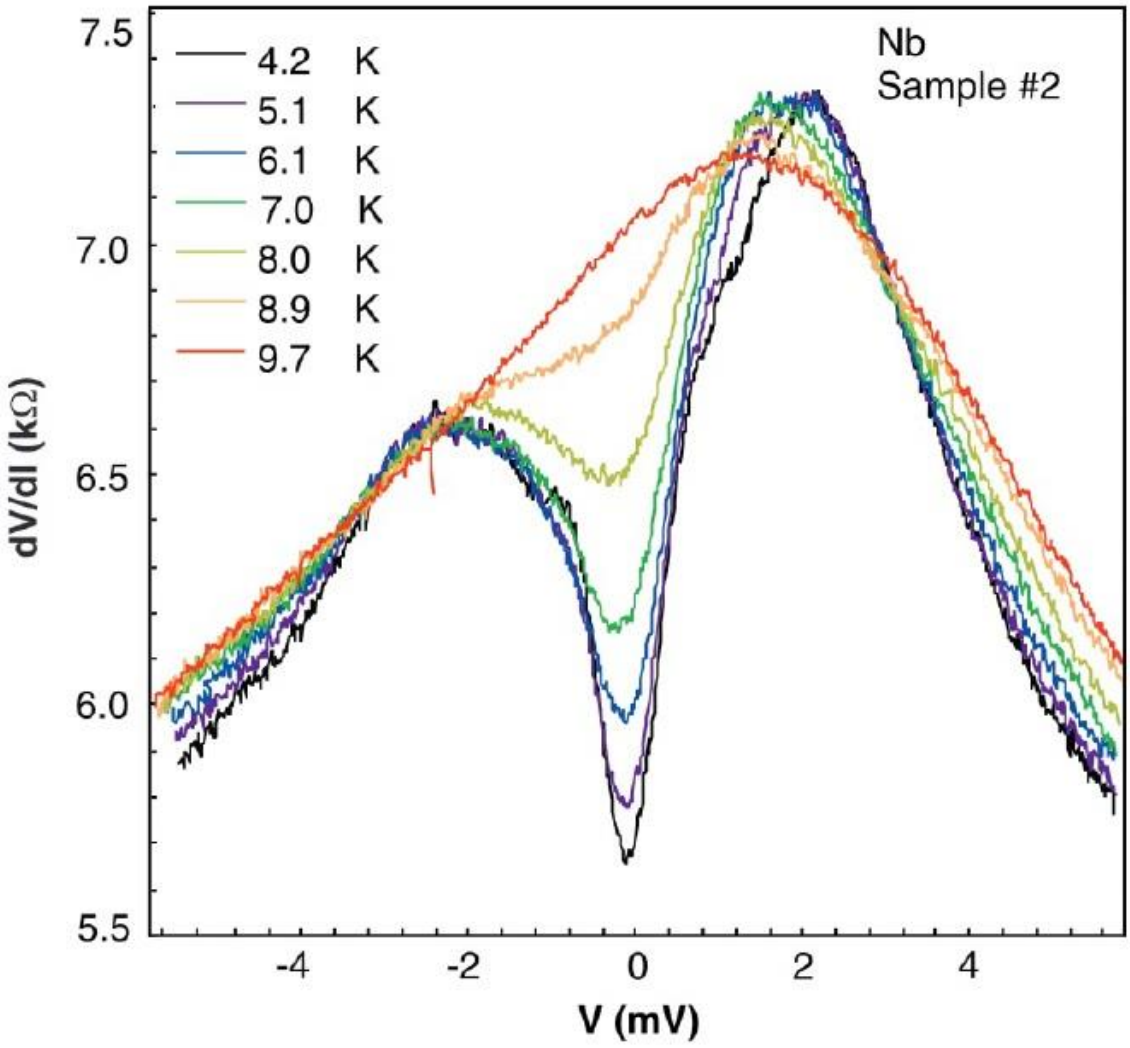

Figure 15 – Differential resistance $\frac{dV}{dI}$ between niobium contacts on carbon nanotube. Superconducting proximity effect features at low bias are more pronounced at low temperatures and vanish above $T_C \approx 9$ K. Image courtesy of [75].

If two superconducting interfaces are placed within close proximity of each other, then the superconducting wavefunction may remain coherent across the normal metal as a zero-resistance supercurrent channel [71]. This kind of device is called a Josephson junction. Supercurrent in exfoliated graphene was explored in 2007 using Al contacts and phase coherent electronic transport was demonstrated [72]. Other carbon-based materials such as nanotubes have also been shown to support supercurrent [73], lending credence to

the notion of making a superconducting Josephson junction using epiGNR in this dissertation work. Even if supercurrent cannot be established, we should still see Andreev reflection from both superconductor/epiGNR interfaces that increases the zero-bias conductance (decrease in differential resistance $\frac{dV}{dI}$) like that shown in Figure 15.

S-wave superconductors exhibit the simplest form of superconductivity that dominates in materials like Al, however more exotic carrier-phonon relationships exist in other materials. In *p*-wave (spin-1) superconductivity there can be pairings of electrons that have the same spin, allowing for three possible combinations of spin giving the pseudo-particle the name of 'spin triplet' [74]. A spin triplet can coexist with a magnetic field as both spins can simultaneously align in one of the triplet states. However, *p*-wave superconductivity is itself a complicated phenomenon, so in discussing a complicated material like epiGNR it is best to restrict ourselves to simpler discussions of *s*-wave superconductors alone.

3.1.2 BTK model

We seek to develop a formal model for the superconducting proximity effect at the SC/NM interface. The interface will act as a scattering barrier of strength Z and, depending on the electron energy and temperature, it will alter the expected Andreev reflection result [75]. A full theoretical model was developed by Blonder-Tinkham-Klapwijk (BTK theory) [76] that uses transmission and reflection probabilities of an incident electron to find a full description for the conductance of the interface. Specifically, on the normal metal side, function A represents the probability for Andreev reflection while function B represents the normal reflection probability. On the

superconductor side of the interface, functions C and D represent normal transmission probabilities for electron and hole-like quasiparticles, respectively. These four functions are the only possible outcomes of an incident electron, so the sum of their probabilities must be one for a given incident energy E and barrier strength Z,

$$A(E,Z) + B(E,Z) + C(E,Z) + D(E,Z) = 1. \quad (12)$$

The functions A, B, C, and D can be found by applying the wavefunction boundary conditions and noting that there is a distinct discontinuity at Δ_{SC}. When the incident energy is within Δ_{SC}, there will be no electron state to transmit to on the superconductor side, so only the normal and Andreev reflection probabilities survive. Above Δ_{SC}, all four functions are non-zero and their expressions are summarized in Table 4. Here, u_0 and v_0 are wavefunction amplitudes for electron and hole states respectively and are functions of just E and Δ_{SC}. When $E > \Delta_{SC}$, u_0 and v_0 are complex and the probabilities are normalized by $\gamma^2 = [u_0^2 + Z^2(u_0^2 - v_0^2)]^2$. As all these functions are known from the boundary conditions, BTK becomes a powerful mathematical modeling tool for quantifying the role of Andreev reflection at the SC/NM interface.

Table 4 – BTK transmission/reflection probabilities. A is the Andreev reflection coefficient and is reduced at low E by a large Z.

	A	B	C	D
$\lvert E\rvert < \Delta_{SC}$	$\frac{\Delta_{SC}^2}{E^2 + (\Delta_{SC}^2 - E^2)(1+2Z^2)^2}$	$1 - A$	0	0
$\lvert E\rvert > \Delta_{SC}$	$\frac{u_0^2 v_0^2}{\gamma^2}$	$\frac{(u_0^2 - v_0^2)^2 Z^2 (1+Z^2)}{\gamma^2}$	$\frac{u_0^2(u_0^2 - v_0^2)(1+Z^2)}{\gamma^2}$	$\frac{v_0^2(u_0^2 - v_0^2)Z^2}{\gamma^2}$

When looking for the interface conductance, we consider the effect of bias voltage across the system. If the superconducting contact is smaller than the mean free path of the materials on both sides of the interface, then it can be considered a ballistic point contact and inelastic scattering can be ignored. The incident electrons from either side of the interface can then be simply described by equilibrium Fermi-Dirac equations. An applied bias voltage will shift the energy of the normal metal side with respect to the superconductor side such that spectroscopic information can be obtained.

The current I across the SC/NM interface is composed of forward and backward contributions. The derivative of the resultant $I - V$ curve then represents the differential conductance spectrum $G(V)$, where V is the bias voltage. By using Eq. (12) to eliminate C and D and dividing $G(V)$ by the normal state conductance G_n we obtain a full equation for the normalized differential conductance [76]

$$\frac{G(V)}{G_n} = (1 + Z^2) \int_{-\infty}^{\infty} \frac{df_0(E - eV)}{dV} [\,1 + A(E) - B(E)]dE, \tag{13}$$

where f_0 is the equilibrium Fermi-Dirac function. At low temperature ($T \to 0$), $\frac{df_0(E-eV)}{dV}$ is a Dirac delta function that is zero everywhere but $E = eV$. At higher T, thermal broadening causes a reduction in the sharpness of the function, especially near $V = \Delta_{SC}/e$.

The superconductor near the SC/NM interface will have a reduced gap Δ_{RPE} caused by the reverse proximity effect. The effect can be modeled by considering an additional layer of superconductor at the interface separating the normal metal from the parent

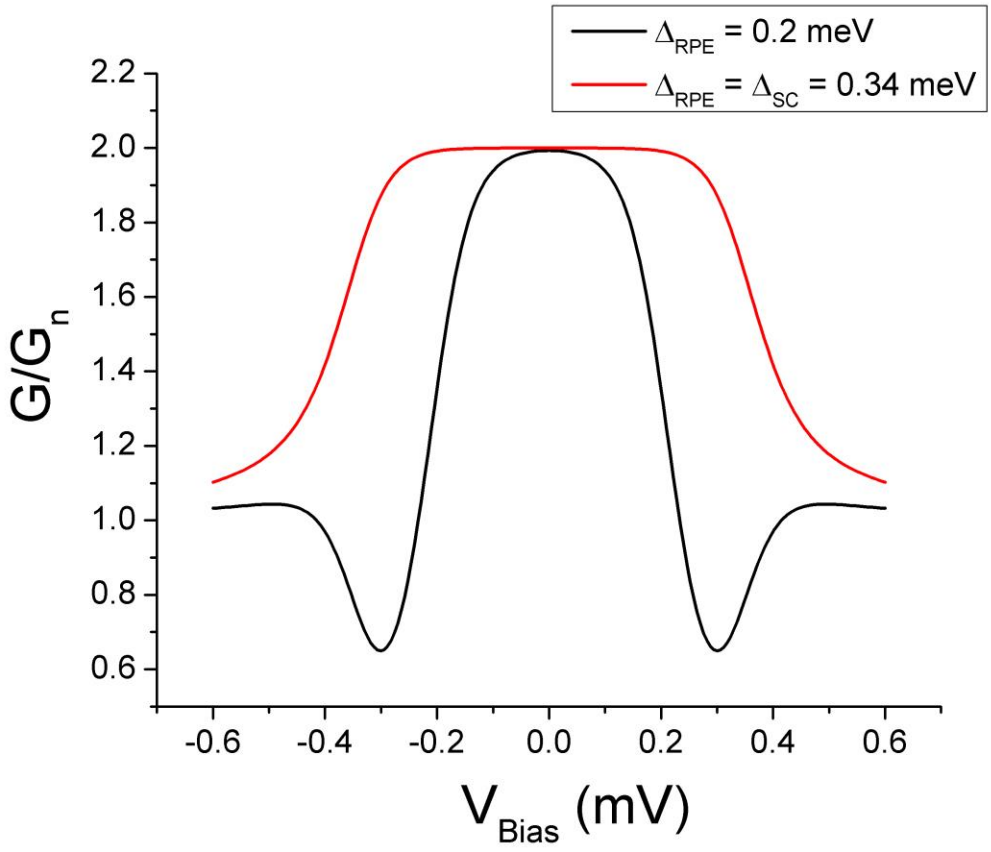

Figure 16 – Extended BTK model considering RPE effect. Parameters used were $T = 0.3$ K, $\Delta_{SC} = 0.34$ meV, and $Z = 0$. The black curve also includes a $\Delta_{RPE} = 0.2$ meV that represents RPE, which manifests as a dip in normalized differential conductance between the two gap energies.

superconductor. Consequently, Δ_{RPE} is always smaller than Δ_{SC}. Adding this consideration to the BTK model requires special treatment of the energy region between Δ_{RPE} and Δ_{SC} as well as two pairs of wavefunction amplitudes u_{01}/v_{01} and u_{02}/v_{02}. In this in-between region both Andreev reflection and quasiparticle transmission are suppressed, resulting in a dip in the conductance spectrum. This dip is shown in Figure 16 where we compare simulated BTK conductance spectra with and without a RPE gap reduction.

3.1.3 Superconductor/Ferromagnet Interface

A bulk superconductor will reject a magnetic field through the so called Meissner effect [77]. The magnetic field lines will bend around the superconductor until the magnetic flux density is so great that the associated energy exceeds Δ_{SC} and the material goes normal to allow the field to pass through. Once the field is reduced below the critical field (B_C), the material will once again repel the field lines and transition to a superconductor. This effect is a consequence of the rigidity of the superconducting wavefunction, whereby the momentum vectors of Cooper pairs have long-range order, causing the wavefunction to remain unchanged by the presence of an externally applied magnetic field [78]. A material with a high degree of spin polarization amongst its charge carriers will break this long-range order and resist the effects of superconductivity [79]. Spin polarization and *s*-wave superconductivity are incompatible when the exchange energy is much larger than Δ_{SC}.

To model the interface between a superconductor and a ferromagnet we modify the BTK model to include spin polarization, following Ref. [80]. The conductance is broken into two parts, a polarized and an unpolarized conductance (G_p and G_u) according to spin polarization P:

$$G = (1 - P)G_u + PG_p. \tag{14}$$

A new table like that shown in Table 4 can be derived but with both polarized and unpolarized versions of each function [80]. Some model examples are shown in Figure 17. By examining the effects of the different parameters, it becomes apparent that Z and P both similarly affect the zero-bias conductance (reducing it from $2G_n$). Differentiating between the two requires analysis of the two satellite peaks that accompany a high Z. It

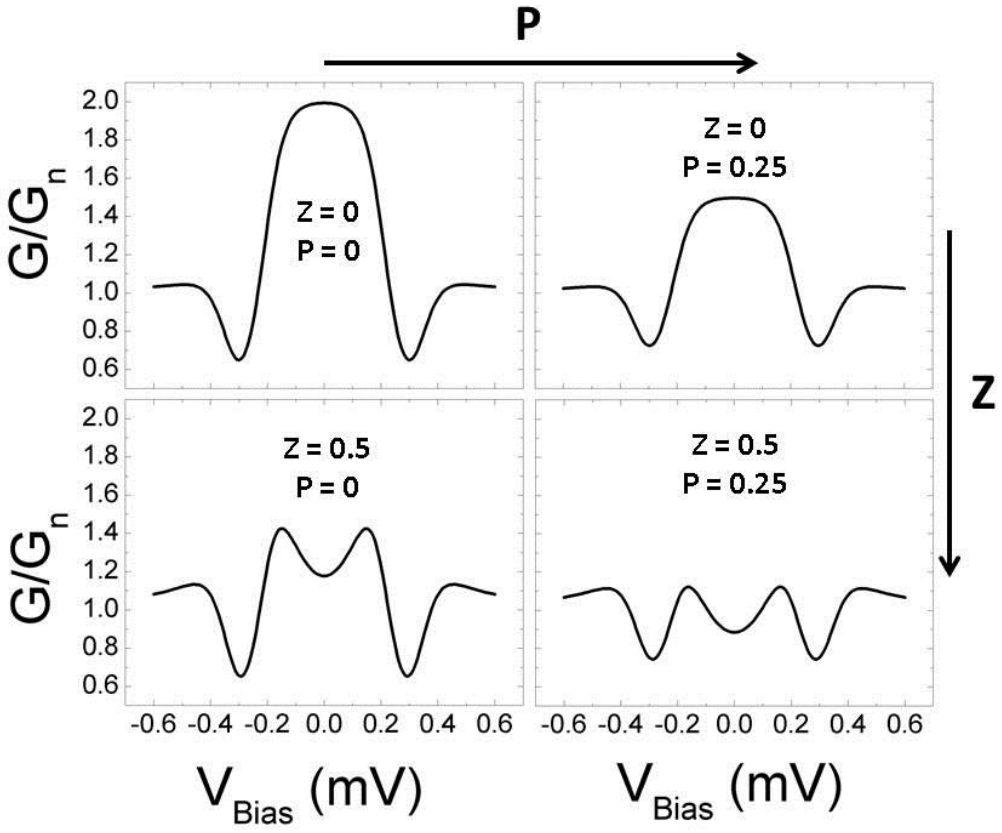

Figure 17 – Extended BTK model using parameters Z and P with $\Delta_{SC} = 0.34$ meV and $\Delta_{RPE} = 0.2$ meV. In all cases, Z and P reduce the zero bias conductance, possibly below G_n for high Z and/or P.

is therefore important to have a transparent interface to accurately measure the spin polarization of a device. With these theoretical tools at our side, we can compare the extended BTK model to a measured conductance spectrum taken with superconducting contacts in order to probe the ferromagnetic nature of the material (in our case, the epiGNR).

3.2 Measurement

Superconducting (*s*-wave) contacts provide a method of interacting directly with the spin asymmetry of the epiGNR channel [79]. By placing two contacts closely

together on epiGNR we attempt to form a Josephson junction-like device, expecting complications due to the previous transport measurements [39]. In general, we should expect the two effects (*s*-wave superconductivity and spin polarization) to conflict and produce a high resistance state.

3.2.1 Metal Stack

Theoretical considerations like the BTK model make it clear that low interface resistance is highly desirable for accurately modelling Cooper pair injection [75]. Pd provides good adhesion to the surface as well as minimizing the scattering barrier upon injection into the graphene [54], however a thick layer of Pd will also reduce the superconducting gap via the RPE. Experimentally, we find that electron beam evaporation of a 5 nm layer of Pd is sufficient for making transparent contact, as explored in Section 2.3.1, without substantially affecting the superconducting properties of the interface.

Achieving the highest T_C possible for our deposited Al contacts greatly improves the coherence length for the superconducting wavefunction [65]. Any impurities in the bulk superconductor either reduce the superconducting gap or broaden the superconducting phase transition. With this in mind, a fast deposition of 5 Å/s at low pressure (~10^{-6} Torr) of extremely high purity Al (>99.999%) will result in a more effective experiment. Oxidation of Al after deposition is also a large concern, so the contacts are either deposited very thick (70+ nm) or capped with 5 nm of Au (using a 5 nm titanium adhesion layer between Al and Au). This way, the bulk Al near the contact

point is never exposed to atmosphere and oxidation of the interface should be at a minimum.

Alternative superconductors were explored, however most required a sputter deposition rather than an evaporation, which resulted in damaged ribbons with poor conduction. A possible solution to this problem is to deposit a layer of Pd via evaporation to protect the ribbon before sputtering materials like niobium or tantalum. However, making the Pd layer thicker will further reduce the superconducting gap and exposure to air between the evaporation and sputtering will contaminate the interface. For these reasons, and because the quality of our sputtered thin films was found to be lacking, plans to use sputtered materials were discarded in favour of electron beam evaporated Al contacts.

3.2.2 Helium-3 Fridge

In the field of low temperature physics, liquid helium is a staple substance, and its rising cost is a significant issue. With a boiling point of 4.2 K, helium-4 (^{4}He) has been the workhorse for cooling systems down to cryogenic temperatures in recent decades, especially in the superconductor sciences that require taking a bulk substance down to single digit Kelvin temperatures. However, to achieve $T_C = 1.2$ K needed for the Al superconducting transition an even colder temperature is required. ^{3}He, an isotope of ^{4}He with a boiling point of 3.2 K, is another useful cryogenic liquid. While the lack of a large accessible ^{3}He supply on earth makes it an expensive substance, it was used in this dissertation as a means to reach temperatures at which Al is superconducting. By pumping on liquid helium with a vacuum pump, the hottest particles boiling at the

surface are removed and the temperature can be reduced even further. Specifically, pumping on ^{4}He can reach 1.4 K while pumping on ^{3}He can provide us with 0.3 K, the base temperature of our proximity effect experiment.

Combining ^{3}He with ^{4}He cryogenics is done in two ways. The most expensive method, a dilution fridge, bubbles the ^{3}He through the ^{4}He to achieve temperatures as low as ~1 mK. The method used in our experimentation is a simpler version that completely isolates the ^{3}He bath from the ^{4}He in its own contained line. This setup uses ^{4}He to condense ^{3}He into liquid such that it falls down to make thermal contact with the sample chamber. Then, a passive charcoal pump is employed to pump the ^{3}He vapor out and lower the temperature of the sample to the base temperature of 0.3 K. A temperature controller is used for the heaters on the sample stage and charcoal pump as well as monitoring the various thermometers in the system.

The superconducting magnet used in the experiment coils around the sample chamber at the bottom of the ^{4}He bath. A separate superconducting shunt provides the switch through which current persisted in the magnet. A heater is applied to the shunt, turning it normal so that current can be injected directly into the magnet. When the heater is turned off, the shunt will turn superconducting and the current in the coil will be trapped in a full loop without dissipation, allowing for a persistent magnetic field. Our equipment can achieve a powerful magnetic field of up to 14 T that is very uniform across the dimensions of the sample. In order to sweep the magnetic field through a range of field strengths the heater must be left on so current can be added or removed from the coil, which consequently boils the helium at a faster rate. Another consideration is that it can be difficult to tell the true zero for the magnetic field as magnetic flux can be

trapped in the coil. In fact, using the superconducting transition for the Al contacts on the sample itself is the most convenient and accurate way to tell the field zero. This is done by sweeping the magnetic field using a bipolar power supply and recognizing that the critical field ($\pm B_C$) should be symmetric about the field zero (see Figure 19). With these factors in mind, the ^{3}He fridge and magnet make a useful measurement setup for our samples.

3.2.3 2-point and 4-point Electronic Measurement

The epiGNR sample is mounted to custom stages and put under vacuum ($\leq 10^{-5}$ Torr) with temperatures ranging from 0.3 K to room temperature. The contacts are thermally anchored through wiring at different temperature stages of the fridge. These wires are then connected to a breakout box with groundable BNC connections and, using a lock-in amplifier with a load resistor, current is injected into the sample through the contacts. The Al contacts stretch across the epiGNR, having an isolated pad on either side. This allows for measurement of the superconducting transition across pure Al, *e.g.*, a 2-point measurement of contacts 1 and 3 in Figure 18, as a control for the Al/Pd/epiGNR junction. Pairs of these dual sided contacts are placed along the length of the ribbon. These pairs potentially make Josephson junctions, with the epiGNR as a normal conductor sandwiched between two superconductors. If the channel is shorter than the superconducting coherence length and the epiGNR is not spin polarized, then we should observe a supercurrent through the entire graphene device.

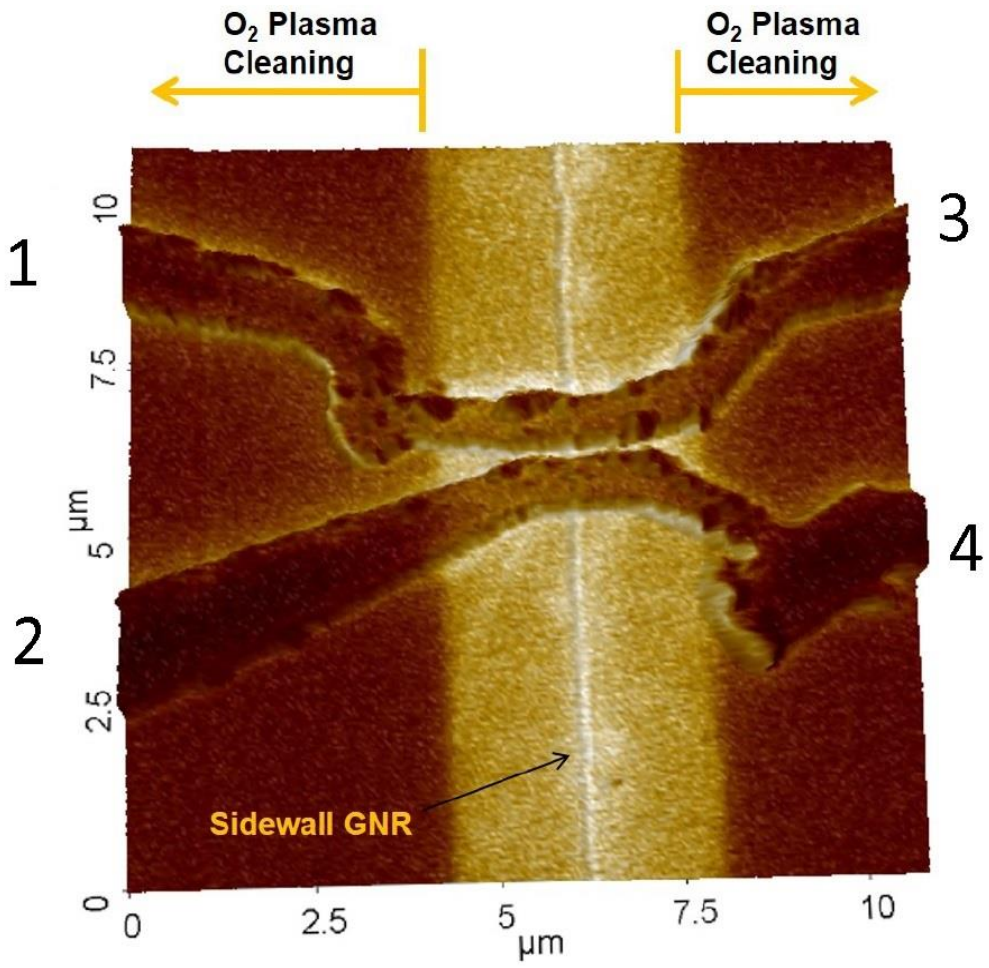

Figure 18 – Al contacts on epiGNR. EFM amplitude contrast overlaid on a 3D topograph of the device area. Contact spacing is 1 micron and the junction is studied using an AC+DC 4-point measurement at 0.3 K. For example, one can run current from contact 1 to 2 while measuring voltage with contact 3 and 4.

When measuring an electrical device, while it can be convenient to use just one injection point (source) and one ground (drain), such a simple 2-point measurement of this nature can often introduce additional complications to the data coming from the resistance of external wiring. By separating the current and voltage paths, such that there are $I\pm$ and $V\pm$ for a total 4-point measurement, just the device in question can be measured. This is because the total resistance will only be a sum over regions where the current and voltage paths overlap so the isolated current and voltage leads will not

contribute to the measured resistance. Many potential measurement configurations use this fact, especially when one considers using the graphene ribbon itself as a voltage or current lead. However, for this experiment full advantage was taken of dual sided Al contacts, as in Figure 18, such that the overlapping region of voltage and current paths includes only the epiGNR channel and the metal stack just above the graphene. The resulting junction is therefore described as Al/Pd/epiGNR/Pd/Al without any influence of outside wiring.

The injected signal is a combination of direct and alternating current (DC and AC). These two components are added in a home-built summer before being sent through a load resistor, such that the respective AC and DC current amplitudes are known. The summer is powered by a pair of 12 V batteries to reduce 60 Hz electrical noise from the power line. Measurement of the AC signal represents the differential resistance $\frac{dV}{dI}$ of the device at that DC bias, temperature, and magnetic field. The resistance is assumed to be ohmic above and below the superconducting transition with a discontinuity at the critical current.

3.3 Observing the Superconducting Transition

The first observation to be made is that entering the superconducting regime the junction had a distinct change to a lower resistance superconducting state. However, that state was not zero ohms and so the junction cannot be said to be a Josephson junction, as no supercurrent is observed through the epiGNR. Still, the junction can be modeled as two superconducting interfaces and a graphene channel as independent components in series. The nature of the SC/epiGNR interface can be interpreted by exploring the

transport physics of the junction and employing what we know about the normal epiGNR channel.

3.3.1 Temperature Dependence

The sample was taken to 0.3 K by pumping on a condensed ^{3}He bath using a passive charcoal pump, crossing the T_C of Al close to the theoretical value of 1.2 K and transitioning to a superconducting state. The devices themselves also transitioned, decreasing in resistance by ~4%. Two devices were measured and though one had a conductance of $\sim G_0$ while the other was $\sim\frac{1}{2}G_0$, the transition magnitude was proportionally equivalent (the normalized resistance scales in Figures 20 and 22 are very similar). Using the temperature as a continuous measurement to observe the transition is time-consuming and poses experimental challenges, particularly when the sample is in vacuum. ^{3}He boils off quickly and the temperature becomes unstable when the bath depletes. For this reason, temperature is best used as a discrete measurement, taking superconducting-state data at ^{3}He base temperature and normal-state data at the temperature of the ^{4}He bath.

3.3.2 Magnetic Field Dependence

Upon application of a magnetic field, the Al contacts went abruptly from a zero resistance superconducting state to a normal state near ± 20 mT (Figure 19). This field is the B_C of the Al contacts, and represents the field at which the entire device is normal. The transition of the epiGNR device, on the other hand, occurred in stages. There are two portions to the transition: one with modest slope that begins at the bulk

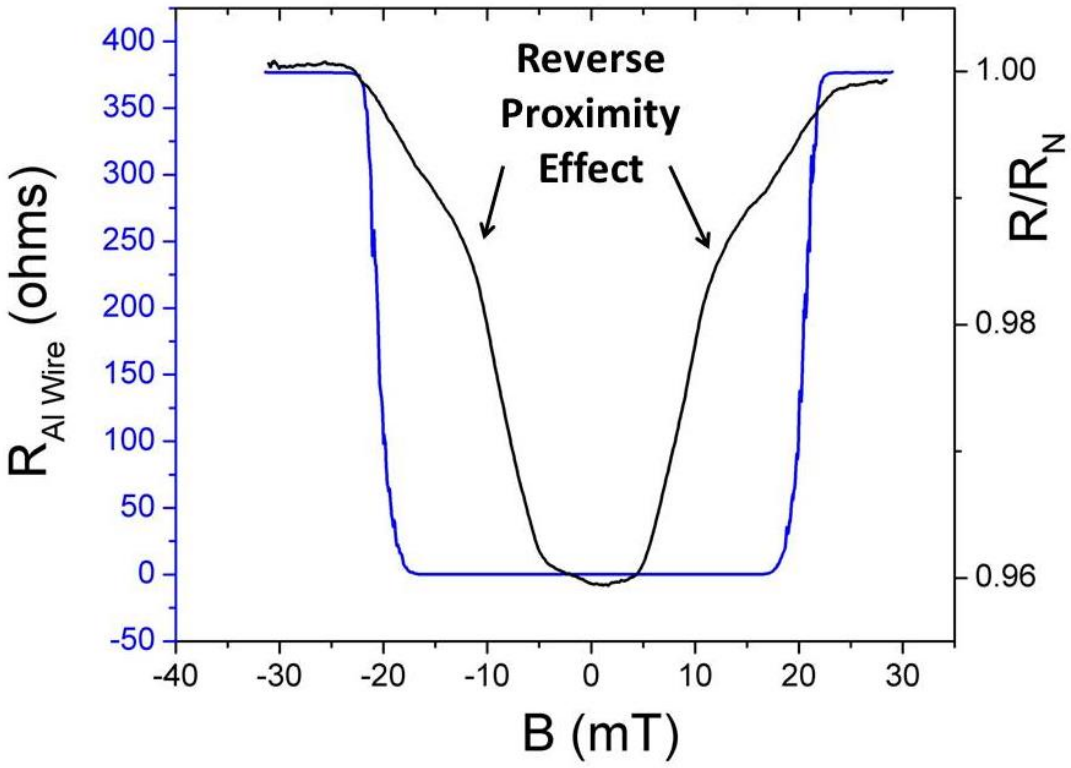

Figure 19 – Magnetic field sweep at 0 V DC bias. The blue curve shows the critical field in the Al contact. The black curve is the normalized resistance across Al/Pd/epiGNR/Pd/Al junction. The high resistance state at high field is taken as normal-state resistance R_N. The indicated kink is the critical field of the reduced gap near the interface due to RPE.

superconducting transition and another with abrupt slope at a lower field, as marked the arrows in Figure 19. Having two critical fields in this way is very suggestive of the proximity effect, as a more fragile, proximity-induced superconducting gap is expected near the Al/Pd/epiGNR interface. The Cooper pairs that are participating in Andreev reflection in the graphene begin to break at lower field while those in the bulk survive up to 20 mT.

The magnetoresistance of the epiGNR channel leads to a large increase in resistance at $B > 1$ T [39]. At low B, however, the change in epiGNR resistance due to

the weak localization effect [81] is negligible or negative [82], as shown in other epiGNR devices [39]. The gradual increase in magnetoresistance within ± 4 mT in Figure 19 is likely to be the magnetic response of the Al/Pd/epiGNR interface whereas the abrupt transition to a higher resistance state between 5 and 25 mT is more in keeping with a superconducting phase transition. As the signal is clear and consistent, exploring the superconducting transition further using a magnetic field sweep is a fruitful approach.

3.3.3 Bias Dependence

The magnitude of DC current through the junction is a convenient parameter to adjust directly using a source meter. By keeping the current low, we can avoid significant local electronic heating in the ribbon and at the Al/Pd/epiGNR interface such that the measurement is in the linear response regime. The applied DC current leads to a voltage bias V_{bias} across the junction which can be measured directly using the voltage probes $V \pm$. However, V_{bias} is also expected to cause local gating in the ribbon, resulting in a change in resistance due to the varying density of states. It is worth noting that sweeping V_{bias} has reproducibility concerns. In addition to a hysteretic effect caused by charging and discharging [83], sweeping V_{bias} across an epiGNR device has at times resulted in an abrupt state transition such that the measured resistance was unreproducible. This may be caused by a physical change in the device, whether at the interface or in the epiGNR channel, as a result of electromigration [84]. Still, some devices were explored in this way and superconducting features were observed. However, gathering data by sweeping the magnetic field and stepping the bias voltage in one direction was a far superior way of observing the superconducting transition and minimizing the effect of voltage hysteresis and unstable measurements.

Stepping V_{bias} through a set of values and doing a continual sweep over the magnetic field resulted in a descriptive set of data for the device. The transition signal devolved into a flat line at high bias as the strong electric field overcame the superconducting gap. Interestingly, however, the transition flipped signs at finite bias voltage, going from a negative change ($R - R_{normal} < 0$) to a positive one ($R - R_{normal} > 0$). This sign change was observed in all samples measured. Further analysis of these spectra is reserved for the next section.

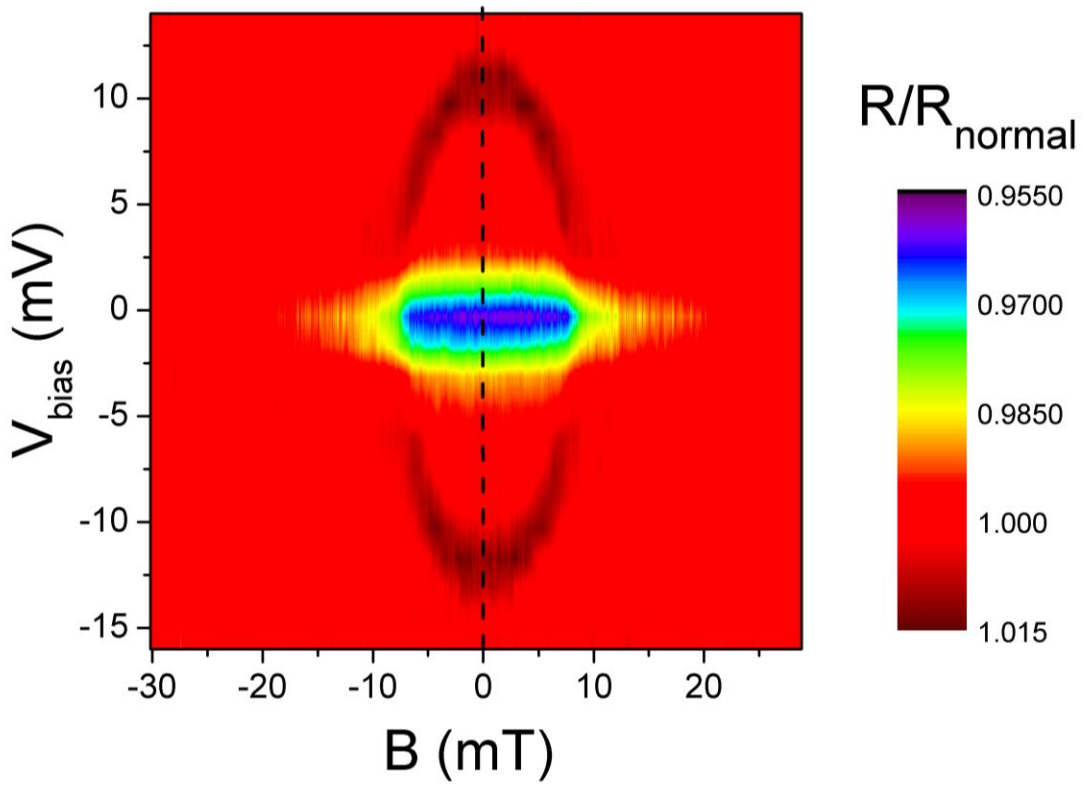

Figure 20 – Contour plot of the normalized resistance $\frac{R}{R_{normal}}$ as a function of magnetic field and bias voltage. The red areas are in the normal state while colored areas are in a superconducting and/or proximity effect induced state. The dark red satellite ring has higher resistance than the normal state and is interpreted as the proximity effect conductance dips in the extended BTK model (Figure 17). The dotted line indicates a zero-field cut shown in Figure 21.

3.4 Results and Discussion

The spectra obtained by discrete V_{bias} and continuous magnetic field dependence are most readily portrayed in a multidimensional representation like a contour plot, see Figure 20. As each spectrum contains over a thousand data points (including at least two forward and backward magnetic field sweeps per V_{bias} step, producing the final contour plot includes several tasks. These tasks include centering the data with respect to zero magnetic field, smoothing the data using window averages, normalizing each curve by the normal state resistance at that bias voltage, and interpolating such that each spectra contains the same number of points. The end result is a succinct visual representation and a properly normalized zero-field bias dependence ($\frac{G}{G_n}$ vs. V_{bias}). This simple curve (Figure 21) is very informative as the conductance dips and zero bias conductance peak are quite visible and ready to compare to the extended BTK model. Using the cleanest set of data taken, further analysis and modeling of the bias dependence is performed.

3.4.1 Comparison to BTK Model

The majority of the junction resistance occurs in the epiGNR channel rather than at the superconducting interfaces, making it difficult to model the junction quantitatively using BTK theory. Still, we normalize the superconducting device resistance by dividing out the normal state resistance at fields above B_C, a normalization process that assumes a small channel resistance. While this invalid assumption prevents quantitative analysis, the qualitative features can still be explored.

When comparing the extracted zero-field conductance spectrum (see Figure 21) to the extended BTK model, the fitting parameters are Z, P, and Δ_{RPE}. The superconducting gap in Al is taken to be Δ_{SC}= 0.34 meV [85] while the temperature is 0.3 K, see Figure 16 and Figure 17. The introduction of Δ_{RPE} produces the observed dips near $V_{bias} \approx \pm 10$ mV, indicative of a region of superconductivity near the interface caused by RPE. The zero bias conductance peak can be attributed to the proximity effect, specifically the Andreev reflection process, but its width seems much narrower than that

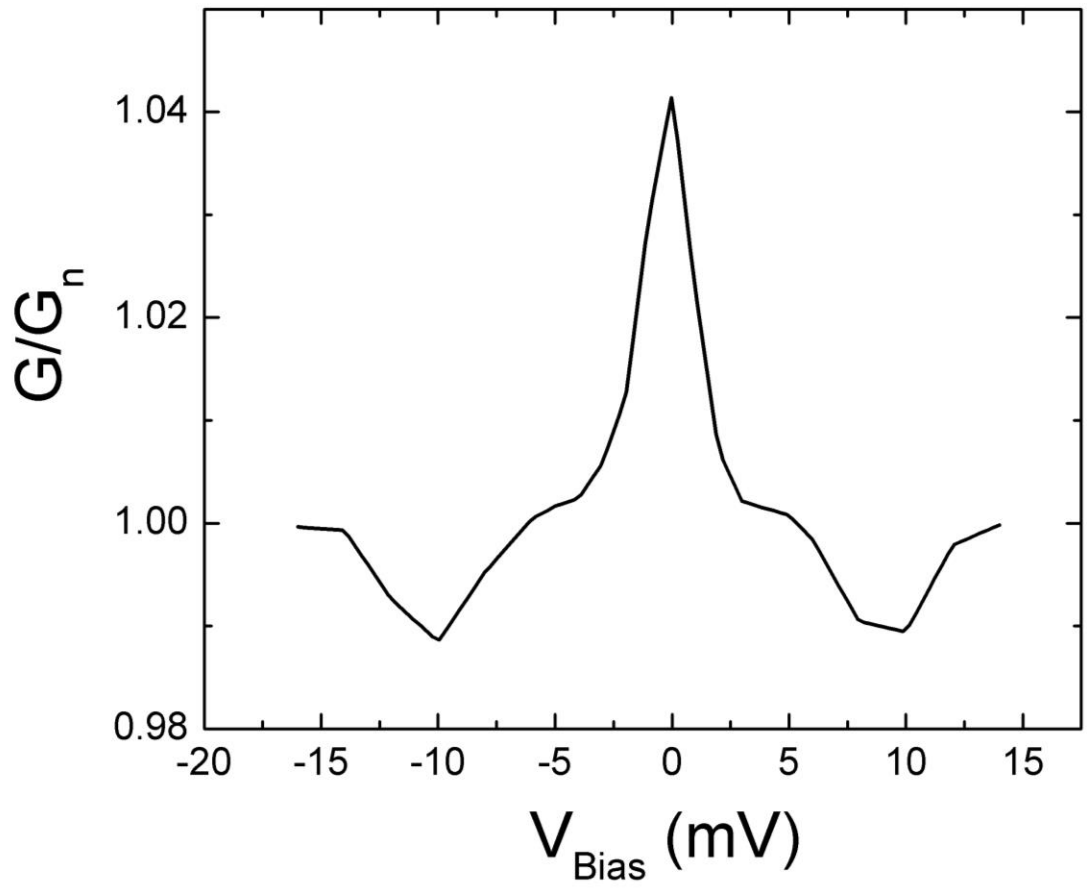

Figure 21 – Extracted zero-field conductance spectrum across an Al/Pd/epiGNR/Pd/Al junction. Andreev reflection causes a zero bias peak while RPE results in conductance dips below G_n. Deviations from the extended BTK model occur due to scattering and resistance of the epiGNR channel that separates the superconducting contacts.

shown in Figure 17. It is important to note that a spectral lineshape like this has been seen before in other proximity coupled junctions, such as quantum well structures [86]. Scattering in the channel reflects the charge carriers back at the superconducting interface in a process similar to multiple Andreev reflection [87]. Both theory [87] and experiment [88] have shown that when the interface transparency is further improved, fine structure (a conductance plateau or a zero bias dip) should appear within the peak. This understanding limits the potential for estimating the spin polarization of the epiGNR channel with this device.

3.4.2 Implications for epiGNR

There are several potential factors limiting the application of these experimental results. The presumption of scattering when analyzing the experiment implies that the similarity of the device conductance to the conductance quantum was coincidental. The source of this scattering could be introduced during the lithography process. Additionally, LFM imaging of sidewall epiGNR like that used in this experiment has shown branching off the main graphene ribbon into side branches that grow on the natural steps caused by the miscut angle (Section 2.2.2 and Figure 10). These branches could scatter the carriers, producing lower than G_0 conductance and reflection like that seen in this proximity effect experiment. Results taken from an epiGNR device with a normal state conductance of G_0 is shown in Figure 22. As one can see, the measured contour plot shows similar patterns as that in Figure 20 and the extracted zero-field conductance spectrum is very similar to Figure 21 in that it has RPE dips and a zero bias peak. The reduced distance between the dips in this junction can be attributed to its

lower channel resistance (compared with the $\frac{G_0}{2}$ epiGNR device shown in Figure 21), as the majority of V_{bias} is across the epiGNR channel rather than the Al/Pd/epiGNR interface. Unfortunately, this device suffered from instability so fewer measurements were taken.

The Al/Pd/epiGNR/Pd/Al junction showed significant proximity effect and a zero bias conductance peak. This observation is, unfortunately, ambiguous as the high resistance of epiGNR and the narrow width of the zero bias conductance peak prevent further quantitative analysis using BTK theory. The extended BTK model implies that if superconductivity has a positive effect on the (zero bias) conductivity of the interface then the spin polarization P is constrained to be $< 50\%$. However, reflections in the epiGNR channel give rise to an additional a quantum interference effect which amplifies the rate of Andreev reflection [87], causing the zero bias peak to become very narrow. While this understanding eliminates the constriction of $P < 50\%$, the observed behavior is still incompatible with the notion of a half-metallic channel in which $P = 100\%$. We note that G_p from Eq. (14) is independent of Andreev reflection in that $A_p(E, Z) = 0$, so only G_u is affected by the amplified Andreev reflection probability. A truly half-metallic channel would not participate in Andreev reflection or RPE at all.

Widening the superconducting gap should reveal fine structures inside the zero bias peak. This fine structure would be more similar to the simulations shown in Figure 16. A higher T_C superconductor would have a larger Δ_{SC} and would overcome RPE more effectively by having a higher Δ_{RPE}. Fitting a more nuanced spectrum with the extended

BTK model should give quantitative results for Z and P, thereby attaining a true measure of the spin polarization in the ribbon.

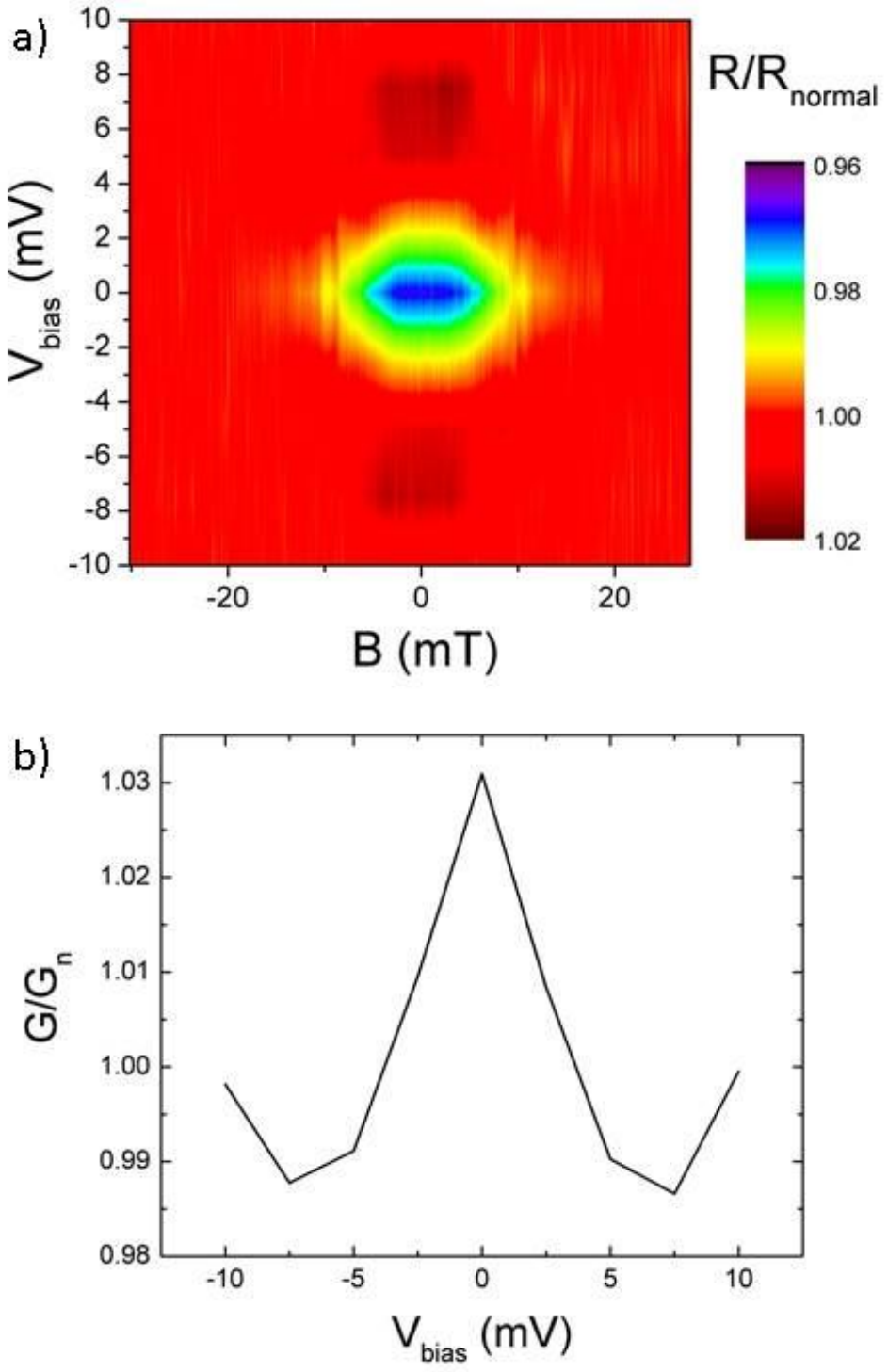

Figure 22 – A second epiGNR junction showing the superconducting proximity effect. The contour plot shown in a) is very similar to that shown in Figure 20. b) is a zero-field extraction like that shown in Figure 21. This junction was less stable and thus fewer V_{bias} steps were taken.

3.4.3 Achieving Supercurrent

Establishing supercurrent in the junction would give access to a variety of measurement techniques for epiGNR spin polarization, in addition to providing proof of concept for an epiGNR Josephson junction [89,90]. Aside from decreasing the channel length until the Andreev reflection regions overlap or lowering the temperature with a dilution fridge, supercurrent may be achieved by altering the electronic properties of the epiGNR channel. While the ground state of charge neutral epiGNR is predicted to be spin polarized [39], the subbands far from the charge neutrality point are not expected to have any ferromagnetic nature [91]. If the channel can be field-effect gated without significant contamination of the ribbon, then these non-ferromagnetic subbands can be turned on such that the channel could potentially support a supercurrent. The ability to change the superconducting proximity effect in the device by tuning the gate voltage would give further evidence for a spin-polarized ground state. Gated epiGNR devices are explored in more depth in Chapter 4 using an Al_2O_3 dielectric and Au contacts.

CHAPTER 4. LOW FREQUENCY ELECTRICAL NOISE

Investigating the carrier density dependence of epiGNR transport provides a wealth of information on topics such as mobility, doping level, and scattering in the channel. Using the field effect, the carrier density can be controlled directly by a gate and the charge neutrality point (CNP) of epiGNR can be probed [8]. Aside from measuring the resistance of a gated epiGNR channel, we also measure fluctuations in that resistance resulting in electrical noise. In addition to the structural information provided by the carrier density dependence [92], the comparable magnitude of the noise is itself a measurement of interest [93,94]. Many device applications, such as sensors [95] and transmission lines, are limited by their signal to noise characteristics.

4.1 Introduction to Electrical Noise

Electrical noise in a transport channel can arise from a number of different physical phenomena. The mean square value of fluctuations in voltage within the channel for a specific frequency bandwidth Δf [96] gives the magnitude of spectral noise $\langle V^2 \rangle = S_V \Delta f$ while the power spectral density S_V will be independent of Δf. In general, S_V obeys certain rules corresponding to the source. These noise sources can be categorized based on the dependence of S_V on the frequency f. White noise, in particular, is independent of f and is mostly dominated by the thermal noise. A channel with resistance R at finite temperature T will black body radiate $k_B T$ energy in per each degree of freedom (with k_B as Boltzmann's constant) and cause a thermal noise in the channel [97] named after the scientists Johnson and Nyquist ($S_{V,JN}$). In thermal

equilibrium, the white noise component of the power spectral density can be shown to have a simple form as:

$$S_{V,JN} = 4k_B TR. \tag{15}$$

4.1.1 Low Frequency Noise

Semiconductor devices have been found to have a dominating noise at low frequencies that has been dubbed 'pink' noise. In fact, noise of this kind has been observed in a multitude of complex systems from electronics to the stock market, and it has been observed in graphene devices as well. These complex systems have been shown to have exponential relaxation effects in the time domain that dominate their low-frequency noise characteristics [98]. The frequency spectrum of such a signal has a Lorentzian lineshape with a characteristic width corresponding to the decay rate of the relaxation. The pink noise can then be described by superposition of these Lorentzian lineshapes with many characteristic frequencies dispersed evenly [94] and the resulting $S_V(f)$ approaches $\frac{1}{f^\gamma}$ for a large range of frequencies. For the ideal, one-dimensional system with exponential relaxations and evenly dispersed decay rates, $\gamma \to 1$. The electrical noise in these systems, being proportional to $1/f$, becomes a limiting factor on low frequency applications [94], making noise characterization an applicable cause by itself.

4.1.2 Noise Amplitude

To compare the $1/f$ noise levels between different materials and experiments, we must find common ground between experimental setups. The power spectral density can

be extracted from a number of electronic measurements including voltage, current, resistance, or conductance, denoted by S_V, S_I, S_R, or S_G, respectively. In each case, the spectral density is proportional to the square of the signal fluctuations so dividing by the square of the signal magnitude will normalize the spectral density across different measurement setups [99]. In this way, one can connect S_V, S_I, S_R, and S_G using:

$$\frac{S_V}{V^2} = \frac{S_I}{I^2} = \frac{S_R}{R^2} = \frac{S_G}{G^2}. \tag{16}$$

With these factors in mind, we seek to find a quantity that can be used for comparison across different materials. First, the thermal noise is calculated according to Eq. (15) and subtracted (or trivially ignored at low frequencies) from the total noise signal measured. The frequency dependence can then be summarized in the negative exponent γ, as previously described. Next, we remove the dependence on f and V from S_V by introducting a quantity describing the noise amplitude A [100]:

$$A = \frac{(S_V - S_{V,JN})f^\gamma}{V^2}, \tag{17}$$

which can be compared across experimental setups and materials from semiconductors to ballistic conductors.

4.1.3 Noise in Graphene

Electrical noise studies have been performed in a variety of graphene systems including exfoliated graphene [99,101], chemical vapor deposition grown graphene [102], reduced graphene oxide [95], and epitaxial graphene [103]. Different research

groups consistently showed a near-$1/f$ dependence to the low frequency noise and the overall noise level in graphene was shown to be competitive with that in semiconductor devices. Boron nitride encapsulated exfoliated graphene, for example, has been shown to have a particularly small value for A in the low 10^{-8} [104]. A more quantitative comparison will be given at the end of this chapter.

Gate-dependent measurements in graphene revealed a non-trivial behavior in A near the charge neutral Dirac point. A characteristic 'M' shape, like the one in Figure 23, was reported by several groups [105-108] wherein the noise amplitude makes a 'V' near

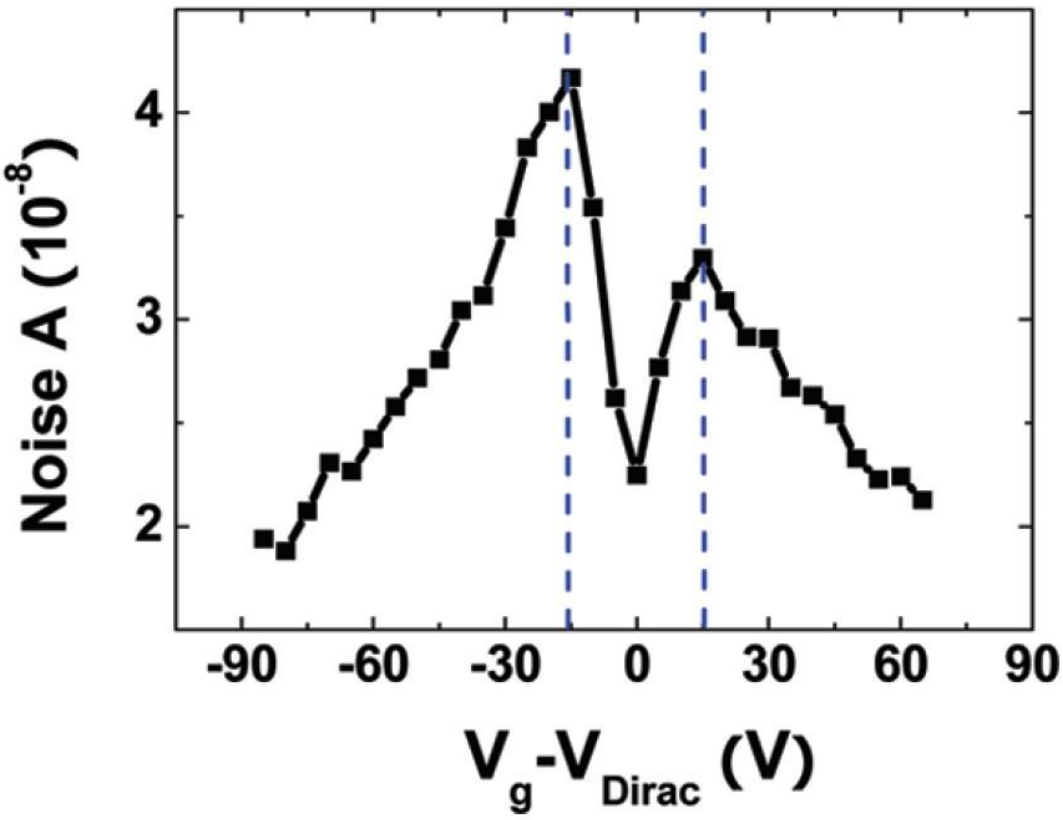

Figure 23 – Characteristic 'M' shape of noise amplitude A measured in exfoliated graphene on silicon oxide. Dotted lines indicate the voltage where the number of free carriers matches the number of charged impurities. Image courtesy of [105].

the CNP and falls off rapidly at higher gate voltages. Such an 'M' shape can be explained as the result of two different types of fluctuations in charge density [105]. For both contributions, it is important to note that small accumulations of charge down the length of the channel will act as series resistors such that their noise spectral densities add: $S_R = S_{R,1} + S_{R,2} + S_{R,3} + \ldots$ [107]. If we assume each charge accumulation independently follows $R \propto \frac{1}{n}$ as indicated by Eq. (3), then Eq. (16) and Eq. (17) imply that small accumulations of charge give large contributions to A. Therefore, far from the CNP mobile charge carriers populate the channel with either electrons or holes and the noise level is low. Near the CNP the mobile carrier density is small, so puddles of electrons or holes will accumulate at charged impurities, defects, or ripples in the graphene and will dominate the transport properties. At the CNP itself, the number of trapped positive charges equals the number of trapped negative charges, such that most charge traps are evenly populated. This results in a noise minimum at the CNP. As the minority puddles deplete, they generate large contributions to the noise, resulting in a maxima in A at the point where the impurity density n_{imp} is on the same order as the carrier density n [105]. The gate acts as a capacitor, drawing n into the channel using an electric field, and thereby allows for a measurement of n_{imp} through the gate voltages that correspond to the peaks in the 'M' shape.

Further analysis can be done by assuming that $S_R \propto (\delta R)^2$ through its fundamental relation to fluctuations in resistance [106] and breaking down δR as follows:

$$\delta R = \frac{dR}{dn}\delta n + \frac{dR}{dn_{imp}}\delta n_{imp}, \tag{18}$$

where the first term gives rise to a dependence of A on $\frac{1}{R^2}\left(\frac{dR}{dn}\right)^2$ and the second term is indicative of the influence of impurity charges on the transport properties of the ribbon. The charge density responsible for the resistance of the device is not necessarily also responsible for the noise signal. In fact, a weak and fluctuating scattering potential may give a negligible contribution to the resistance, but be the dominant factor in the noise [106]. In general, at large values of n the $A \propto \left(\frac{\delta R}{R}\right)^2$ will follow a n^{β} trend, where $-2 < \beta < 2$ depending on whether R or δR dominates. The value of β provides a measure of the type of scattering imposed by n_{imp}, with $\beta = -2$ indicating long-range scattering and $\beta = 2$ indicating short-range scattering [106].

4.1.4 Extrinsic Quantities

Noise measurements on two-dimensional graphene have consistently shown an inverse dependence of A on the square area of the channel [109-111]. This trend is also seen in semiconductors [112], where it is attributed to the volume dependence of the total number of charges N. The Hooge parameter α_H is generated by multiplying A by N and represents an attempt at a new extrinsic quantity that is independent of all experiments [112]. While this trend was well obeyed by one-dimensional carbon-nanotube field effect transistors [113] and it can be useful to employ as a measure of the system, α_H is by no means a universal constant. Many graphene works do not use α_H at all, but rather the noise amplitude multiplied by the square area to characterize the device [104,108,114]. The dependence of the noise amplitude on the carrier density is instead a useful experiment variable and fitting parameter, as per the analysis in the previous

section, providing information about the scattering in the channel. This dependence will be investigated in epiGNR in the following sections.

4.2 Measurement

Back gating and side gating using the substrate as a dielectric have proven useful in controlling the carrier density in a transport channel [115]. However, using the SiC substrate to gate epiGNR has proven to be a difficult challenge [116]. Instead, a top gate that can expose the channel to an electric field is formed by depositing a dielectric layer and an electrode over the epiGNR via the fabrication process outlined in Chapter 2. The carrier density n injected into the epiGNR in this way is proportional to the applied voltage V via the per-area capacitance C_k. By using reliable fabrication and characterization procedures, C_k can be approximated from the formula for a parallel plate capacitor with fringe field correction [117] such that

$$e\,n = C_k V = \frac{\varepsilon}{d} V \left\{1 + \frac{W}{L\pi}\left[1 + \log\left(\frac{2\pi L}{W}\right)\right]\right\}, \tag{19}$$

where W is the width of the epiGNR, L is the length of the channel, ε is the permittivity of the dielectric, d is the thickness of the dielectric, and $\log()$ is the natural logarithm.

4.2.1 Signal Analyzer

A Fourier transform is a well-known integral transform that includes a unitary phasor in the integrand. This transform can be used to relate real space to *k*-space, as in Chapter 1, and to convert time-domain signals to the frequency domain. An apparatus called a 'signal analyzer' will immediately perform a Fourier transform on input signals

and output the signal in the frequency domain. The SR780 signal analyzer utilized in this work can give power spectral density units via automatic division by Δf such that S_V for the epiGNR channel can be recorded through a general purpose interface bus cable for in depth analysis.

In practice, the frequency spectrum of a real signal cannot be known at arbitrarily high and low frequencies because of a finite measuring time and sampling rate [118]. Our experiments are more concerned with low frequencies where $S_{pink} > S_{white}$, therefore the sampling rate is less important than the measuring time. Reducing the size of the binning to achieve resolution at lower frequency results in an increased measurement time. To achieve 125 mHz frequency resolution, for example, a single noise spectrum will take 8 seconds to obtain. Random fluctuations in noise can be prohibitive in making conclusions from a single spectrum, so for most measurements many spectra (~100) were taken in sequence and averaged. As such, the full measurement of a single reproducible spectrum with 125 mHz resolution can take 10-15 minutes to acquire. While this limitation makes measurement difficult, it is not prohibitive. This is especially true during stable, room-temperature measurements that can be done over long time periods.

4.2.2 EpiGNR device

Chapter 3 measured the differential resistance of a superconducting device that had an unknown bias voltage dependence. This approach is more informative when the device is not in the linear response regime, meaning that Eq. (4) does not hold. In the case of an epiGNR channel with normal metal contacts $R = \frac{V}{I} = \frac{dV}{dI}$ as long as the DC

current applied is not causing significant local heating in the ribbon. By measuring epiGNR at different bias voltages, we have shown that this relation is valid at currents under 1 μA. Performing differential resistance measurements requires an AC signal that would be highly visible after a Fourier transform, not just at the operating frequency but also at all of its harmonics. Instead, we use a DC excitation to measure the static resistance and noise of the device.

4.2.2.1 Contacts and Gate

Pairs of metal contacts spaced at 1 μm are placed along an epiGNR with ~4 μm of separation. The entire device area, including the contacts themselves, are covered in dielectric with a top electrode for gating. The epiGNR between each pair of contacts is individually gated, such that there are several independent epiGNR devices along the length of the same ribbon. The devices located farthest away from each other on the graphene channel can be used to inject current into the ribbon beneath the middle devices, such that the graphene ribbon itself can be used for contact to the device of interest. This technique allows for greater choice of measurement modes.

The metal contacts are deposited using electron beam evaporation in a single deposition phase. A 10 nm Pd layer is deposited at 0.5 Å/s as an adhesion layer and for the low scattering upon current injection. A 30 nm Au layer is then deposited at 1 Å/s on top for its non-corrosive and conductive abilities. The gate was made using the process explained in Section 2.3.3, which I briefly describe here. 10 nm layers of Al are deposited at relatively low vacuum (~10^{-5} Torr) and slow deposition rate (0.2 Å) to form Al_2O_3. Three layers are deposited with venting and physical rotation of the sample in

between to assure full oxidation and coverage. The resulting gate dielectric was measured at 41 nm and assumed to have a dielectric constant of 7 [119], resulting in a C_k of 176 nF/cm^2 including the fringe field contribution described in Eq. (19). Lastly, a 30 nm Al layer is deposited at 2 Å/s under normal evaporation vacuum (~10^{-6} Torr) as the gate electrode.

4.2.2.2 Measurement Modes

In measuring both the noise and the resistance, one useful practice is to separate the resistance measurement from the noise measurement. In so doing, one can keep the measurement setup as simple as possible in order to avoid a number of issues discussed in Section 4.2.3 that can influence the electrical signal. In addition, measurement of the noise takes a long time (minutes) while the resistance can be measured nearly instantaneously. As such, in this work the resistance measurement is readily taken before and after the noise measurement to ensure consistency. We thereby obtain both resistance and noise spectra throughout the experiment.

Two types of measurement modes were used in this experiment: 4-point constant current mode and 2-point constant voltage mode. To ensure that the noise of the contacts was not a concern, an external voltage was applied to the ribbon outside the gated area while the inner contacts were used solely for measuring V and S_V. This 4-point constant-current mode, portrayed in Figure 24, provided an accurate measurement of the bias and temperature dependence of the sample. Automating the setup for measurement of the gate voltage dependence required additional complexity and introduced irreconcilable noise into the system unless reduced to a 2-point measurement setup. The voltage divider

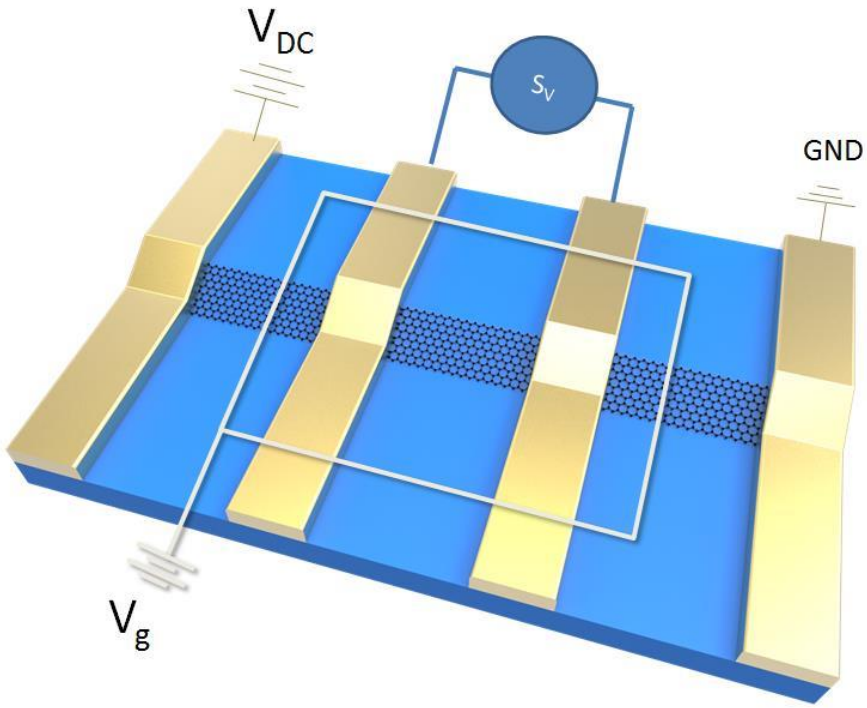

Figure 24 – An artistic representation of a 4-terminal voltage noise measurement on epiGNR. The top gate covers the entire junction area while biasing the channel uses contacts outside the gated area. The image is not to scale and for illustrative purposes only.

caused extraneous noise in the 2-point configuration, so constant voltage mode was used with a current amplifier for converting the measured current into a voltage signal that could be sent to the SR780. As these two measurement modes produced nearly equivalent spectra, the continuous 2-point measurement was performed on epiGNR to observe the gate dependence of the $1/f$ noise.

4.2.2.3 Mobility

The carrier density n and the voltage on the gate V_g are naively correlated via Eq. (19). However, we must address two additional concerns. The first is that the intrinsic

doping level of the epiGNR offsets the carrier density at zero gate voltage ($V_g = 0$). V_{CNP} is the gate voltage at which the number of hole carriers equals the number of electron carriers and is indicated by a maximum in device resistance. To succinctly express this offset, we use $V^* = V_g - V_{CNP}$ with $V_{CNP} = -3.1$ V in the following discussions. The second concern is the quantum capacitance of the epiGNR itself which becomes important at the low carrier densities near V_{CNP}. Combining the correction for quantum capacitance given by Xia et. al. with the geometric capacitance found in Eq. (19) gives

$$V^* = \frac{e}{C_k} n + \frac{2\hbar v_F \sqrt{\pi n}}{e}. \tag{20}$$

The rate at which $R(V^*)$ falls off from the CNP resistance peak is a measurement of the mobility. After accounting for the contact resistance R_C, the resistance curve can be analyzed at high V^* ($n > n_{imp}$) so as to minimize the effects of the impurity density when using Eq. (3). The geometric factors relating R to ρ can be summarized by the factor N_{sq}, which represents the channel length as a number of square areas. Equation (20) can then be inverted to obtain $n(V^*)$ such that R as a function of V^* is given by [120,121]

$$R(V^*) = R_C + \frac{N_{sq}}{n(V^*)e\mu}. \tag{21}$$

4.2.3 Noise Reduction

Electrical noise measurements can be very sensitive to environmental conditions and external electronics. One of the greatest concerns for the stability of the noise signal

is a so called ground loop. This situation occurs when two different grounds are connected across the device wiring, causing continuous current flow and extraneous noise at many frequencies. An isolation transformer can be used to reduce the influence of ground loops, but it is important to keep the circuit as simple as possible with very few electrical components. This will also help to reduce the influence of the 60 Hz line frequency.

With simplicity of components in mind, the DC signal is provided by an isolated battery in a shielding box. Long wires can pick up external disturbances as they act like antennas and could be influenced by radio or cell phone signals. Keeping the wires as short as possible minimizes this risk. If $V+$ and $V-$ are measured, as in the case of a 4-point measurement, the wires are twisted together so any disturbance will affect both outputs in the same manner and thus not affect ΔV. As a final concern, the sample ground is kept from making electrical connection to large metal reservoirs, like the fridge shielding, that may introduce additional noise sources. The ground is connected directly to the root of the core building ground to avoid cross-talk to other electronics.

4.3 Results and Discussion

The epiGNR device was measured at room temperature under vacuum (~10^{-5} Torr) and S_V was recorded with a large number of averages. The number of averages and frequency resolution varied, but each measurement generally consisted of ~100 averages with frequency resolution $\Delta f = 125$ mHz and a frequency range of 200 Hz. Twelve samples were measured for their low frequency noise characteristics. The measured exponent γ varied, but when the setup was stable and properly grounded $0.9 < \gamma < 1.1$ at

room and nitrogen temperatures. This is consistent with that obtained in other types of carbon systems [100,101,110], thereby enabling quantitative comparisons.

4.3.1 Bias Dependence

Biasing the epiGNR channel should change the noise level according to Eq. (17). Though a battery with a fixed voltage supplies the DC excitation, voltage dividers can be attached to reduce the output voltage to a fraction of the battery voltage. A voltage divider is a simple 'T' made with two resistors of very different resistance. Both resistors are connected to the sample, with the larger resistor connected to the voltage source and the smaller connected to ground. The dependence of S_V on f and V is shown in Figure 25 and fit with $S_V = \frac{AV^2}{f^\gamma} + S_{V,JN}$. Bias voltage increases the noise spectral density and causes it to take on a near-$1/f$ shape, while low bias voltage results in a flatter spectrum that approaches $S_{V,JN} \approx 10^{-16}$ V^2/Hz. A cut is taken at 40 Hz and the corresponding S_V is plotted as a function of bias voltage in the inset to Figure 25. This allows us to fit $S_V(V)$ with a simple parabola for the noise amplitude $A \approx 10^{-7}$. Knowing how closely the bias and frequency dependence follow expectation [122], A will be used as a means of comparing epiGNR to other graphene systems in Section 4.4.3.

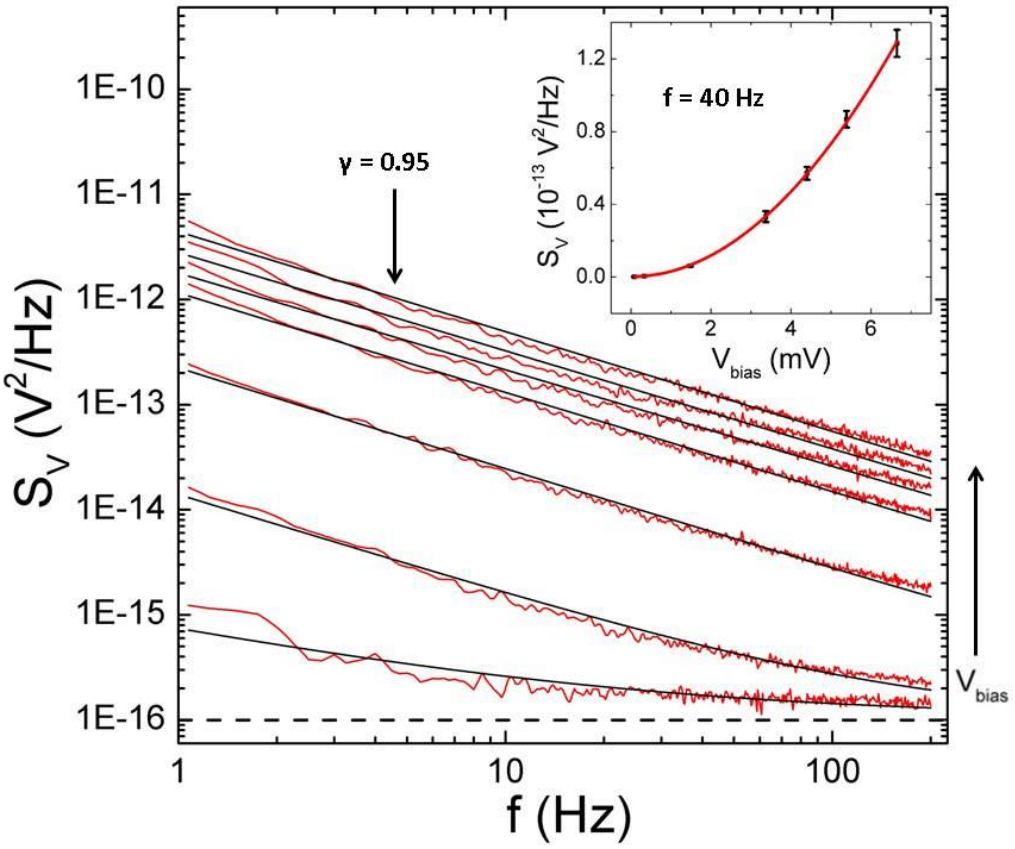

Figure 25 – Bias dependence of noise spectral density measured at 77 K. At high bias, the spectra exhibit a dependence close to the expected $1/f$. At low bias, the spectrum became flattened just above the Johnson-Nyquist level (dotted line). A cut was taken at 40 Hz and fit with a parabola (inset). The quadratic coefficient multiplied by the frequency produces the parameter *A*, which represents the noise amplitude of the device (~10^{-7} or less).

4.3.2 Carrier Density Dependence

Sweeping the gate voltage while monitoring the resistance allowed us to select a device with an accessible CNP to be used for extensive noise measurements. A and R are measured at room temperature and plotted together as a function of V^* in Figure 26. The resistance maximum and the 'M' shape of the noise amplitude coincide at the CNP, while both fall off at large V^*. This gate-dependent transport measurement provides a wealth of information about the scattering mechanisms in the channel. As such, we will analyze

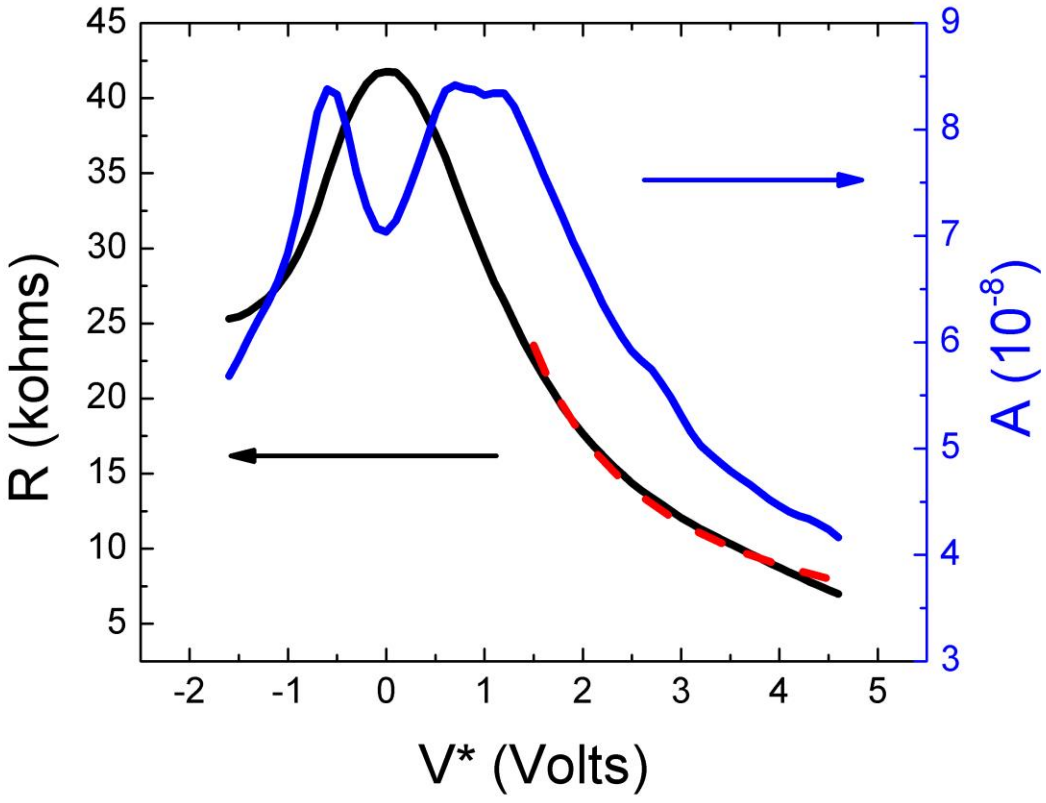

Figure 26 – Resistance (black) and noise amplitude (blue) at room temperature as a function of gate voltage across the CNP. The resistance is fit at high voltage (red dashed line) using a capacitance model that includes a quantum correction. The noise amplitude shows an 'M' shape dependence about the CNP.

both spectra and their implications on epiGNR transport.

Calculating a doping level at zero gate bias in the epiGNR from V_{CNP} and Eq. (20) yields $\approx 3 \times 10^{12}$ cm^{-2}. Far from the CNP mobile carriers flood the ribbon ($n \gg n_{imp}$), dominating its transport properties. By fitting the resistance curve at high V^* with Eq. (21) we obtain $\mu \approx 2066$ cm^{2}V^{-1}s^{-1} and $R_C \approx 1.1$ kΩ. These results are reasonable and consistent with other measurements on Si-face epitaxial graphene [123]. We also note that the width of this ribbon (~100 nm) is large enough that the confinement energy given by Eq. (9) (~21 meV) is less than the thermal energy at room temperature (~26 meV). In this case, we should not expect to see the effect of individual subbands in the epiGNR.

The 'M' shape that $A(V^*)$ takes near the CNP is a result of a shift in dominance between two different electronic mechanisms, as explained in Section 4.1.3. While the transport properties of epiGNR are dominated by n at high V^*, static impurities (n_{imp}) account for the transport phenomena near the CNP. The greatest noise in the channel is generated by patches of minority carrier states that are nearly depleted [105]. This situation occurs when nearly all of those carriers have been annihilated with an equal number of mobile carriers, *i.e.*, $n = n_{imp}$. From Figure 27, $n_{imp} \approx 5 \times 10^{-11}$cm^{-2} can be extracted, shown by vertical dashed lines where positive n corresponds to electron injection and negative n to hole injection.

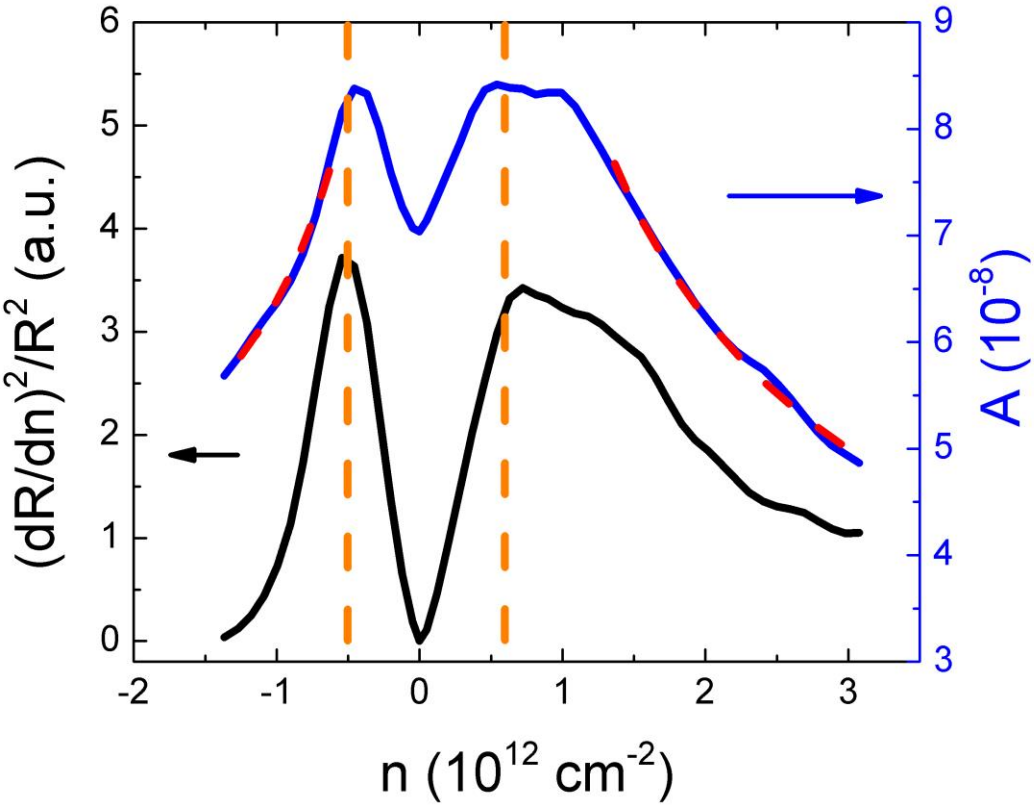

Figure 27 – Noise amplitude (blue) and normalized resistance derivative $(dR/dn)^2/R^2$ (black) as a function of carrier density. A remarkable similarity between these curves is apparent. Orange dashed lines show the estimated impurity density of $n_{imp,e} \approx 6 \times 10^{11}$ cm^{-2} for electrons and $n_{imp,h} \approx 5 \times 10^{11}$ cm^{-2} for holes. Red dashed lines are n^{β} fits for the electron and hole side of the noise amplitude with $\beta_e = -0.38$ and $\beta_h = -0.54$, respectively.

Following the treatment of Section 4.1.3, we look to find a dependence of A on the quantity $\frac{1}{R^2}\left(\frac{dR}{dn}\right)^2$. In Figure 27, we plot the noise amplitude together with the square of the normalized resistance derivative. The similarity is striking, giving credence to the theoretical treatment applied. By fitting the electron side of A with n^{β_e} and the hole side with $(-n)^{\beta_h}$, we can gain useful information about the dominant scattering mechanism in the ribbon. Specifically, we find that $\beta_e = -0.38$ for the electron side while $\beta_h =$

-0.54 for the hole side. These values, similar to those reported in exfoliated flakes [106], point to long-range scattering coulomb potentials, although not in the extreme limit (in which case $\beta = -2$). Long-range scattering (*e.g.*, charged impurities trapped near the graphene/silicon-oxide interface [124]) has an effect on the resistance that is inversely proportional to n while the effect of short-range scattering (*e.g.*, lattice defects) is independent of n. As such, a negative β like that shown in the epiGNR device implies that fluctuations due to long-range scatterers are the dominant contribution to S_R and the strongest source of noise in the channel.

4.3.3 Impurity Density

Charged impurities have been shown to be a large source of noise in carbon systems such as metallic carbon nanotubes [125]. The transport properties of exfoliated graphene near the CNP are dominated by 'charge puddles' caused by interaction between the impurities embedded in the substrate and the graphene sheet [126,127], which are also a noise source [105]. Attempts have been made to reduce these interactions using advanced substrate techniques such as suspended graphene and encapsulation using hexagonal Boron Nitride [128]. Substrate interactions and structural defects are not a concern in epiGNR because of the high growth temperatures and low graphitization rate of the confinement-controlled growth process [13]. Pre-growth annealing as well as the manner in which the epiGNR drapes over the sidewall (Figure 4) also serve to limit the influence of substrate impurities and charge accumulations caused by the growth process. Contaminants introduced during fabrication, however, could be responsible for the noise signal measured. In addition to residues left on the graphene surface after lithography, ions trapped in the gate dielectric during deposition could impose charge accumulations

in the epiGNR. Charged contaminants such as these would produce an effect similar to the puddles created by a substrate interaction [92]. The atmospheric oxidation method used to produce Al_2O_3 likely introduces impurities into the dielectric, such as water and nitrogen. Charged impurities trapped at the graphene/Al_2O_3 interface are thereby considered the strongest source of noise in the epiGNR device.

4.4 Comparison to Other Transmission Lines

By comparing the epiGNR channel to other carbon-based systems, we can evaluate the low frequency performance of epiGNR as a transmission line. Several quantitative measurements are explored across a number of carbon transmission lines and prospects for epiGNR as a high-quality interconnect or chemical sensor are described.

4.4.1 Hooge Parameter

α_H, the Hooge parameter as discussed in Section 4.1.4, is used by many systems as an extrinsic measure of noise that accounts for the number of carriers in the system. Although its validity is under debate [129], it is widely used in the literature and correctly normalizes for the device area. As we have shown in Section 4.3.2, the measured carrier density dependence of the noise amplitude A is non-monotonic, instead following an 'M' shape. Therefore, the corresponding α_H is expected to exhibit the same behavior, due to their straightforward relation $A = \alpha_H/N$. Nevertheless, it is instructive to present an order of magnitude for α_H as for comparison with previous measurements in other systems. Specifically, we find $\alpha_H \approx 10^{-4}$ at $n \approx 10^{12}$ cm^{-2}, making our epiGNR devices competitive for electronics applications in terms of low α_H. We note that in many metals and semiconductors, $\alpha_H \approx 2 \times 10^{-3}$ [112]. Most reports of carbon

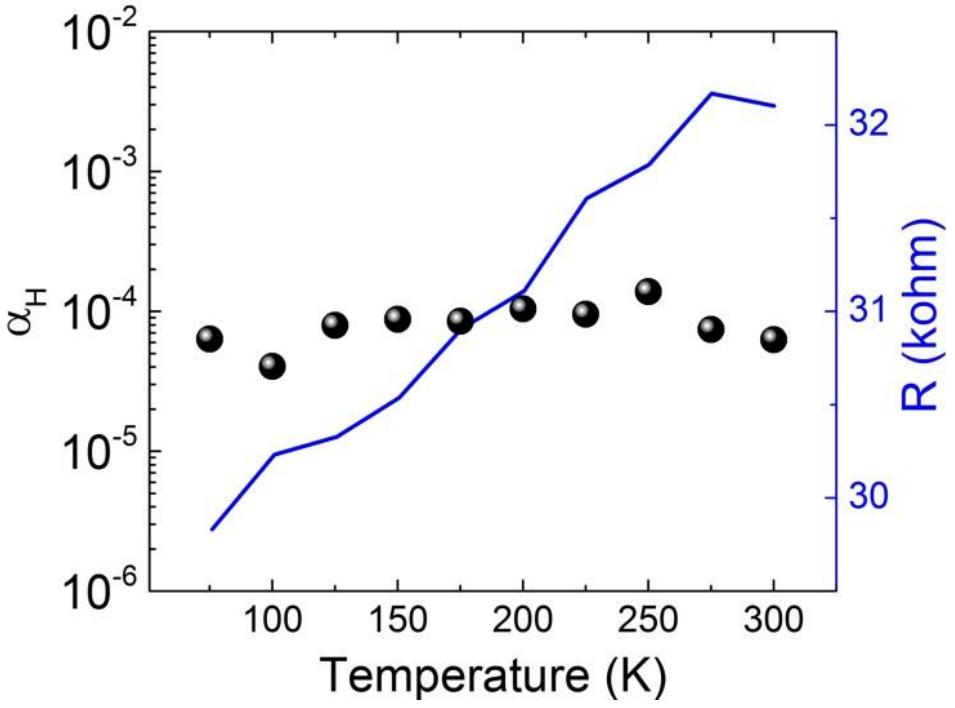

Figure 28 – The Hooge parameter (spheres) remained approximately constant at 10^{-4} throughout the temperature range while the resistance went down modestly at lower temperatures (blue curve). The Hooge parameter was taken at $V^* = 0.95$ V at each temperature (constant carrier density) while the resistance curve was taken at a fixed zero gate voltage.

nanotubes on Si substrates give $\alpha_H > 10^{-3}$ [100] while many single layer exfoliated graphene devices show $\alpha_H \approx 10^{-3}$ or less [110,111]. Multilayer, bilayer, and suspended monolayer graphene have revealed lower noise, closer to our epiGNR value of low 10^{-4} [107,109].

4.4.2 Temperature Dependence

Several groups have shown a monotonic decrease in the noise of carbon systems with decreasing temperature [107,122], evidenced by substantial reduction of the noise spectral density at low temperatures. Noise levels were reduced by as much as two orders of magnitude, for example, in few layer graphene from room temperature [114].

The experiments we performed on epiGNR, however, showed no such dependence (Figure 28). The measurement was taken by maintaining a constant carrier density at each step in temperature. At each measurement step the temperature was manually stabilized to avoid noise generated by the temperature controller, the gate voltage was swept to find the CNP, the results of which are shown in Table 5.

Table 5 – Gate voltage of CNP measured from nitrogen to room temperature. The monatonic dependence indicates a charging/gating effect at low temperatures.

Temperature (K)	Charge Neutrality Point (V)
77.4	-4.45
99.2	-4.19
125.0	-4.16
150.2	-3.81
174.6	-3.87
199.5	-3.66
224.4	-3.49
249.9	-3.43
274.4	-3.23
298.9	-3.17

The noise spectra were taken at $V^* = 0.95$ V for each temperature step, approached consistently from the negative side to avoid hysteresis effects. The Hooge parameter consistently clung to its value of ~10^{-4} for all temperatures measured between room temperature and liquid nitrogen temperature. The temperature dependence of A in graphene devices was shown to separate from carrier dependencies [107] (*i.e.*, $A = g(n)f(T)$), so our observations imply that the sources of noise in epiGNR devices are temperature independent: $f(T) = const$.

4.4.3 Noise Amplitude

Aside from α_H, the noise amplitude A itself has also historically been used as a point of reference when accounting for the geometric area of the device, in that smaller junctions are expected to have a larger A. Our value, $A = 4\text{–}10 \times 10^{-8}$, is also comparable with a variety of graphene studies, especially when accounting for our small device area (~0.1 μm^2). Measurements on single walled carbon nanotubes typically yielded $A > 10^{-7}$ [100,130,131]. Exfoliated graphene encapsulated in hexagonal boron nitride, a structure reported to have a high mobility, showed $A \approx 0.5\text{–}2 \times 10^{-8}$ [104] for devices with channel areas >1 μm^2. Similarly, chemical vapor deposition grown graphene on hexagonal boron nitride shows that larger devices can have $A < 10^{-9}$ [108], but that smaller devices extrapolate upwards of $A \sim 10^{-7}$ for device areas like ours.

Lastly, it has been shown that low frequency electrical noise of graphene can be used for practical chemical sensing, but a low level of $A \sim 10^{-8}$ is required [132]. This requirement may be attainable with epiGNR if long-range scattering centers can be reduced. Reducing the number of contaminants introduced by the lithography and gate fabrication processes, as well as reducing ribbon branchings and edge meandering, will certainly improve the noise levels in the device, making epiGNR a viable candidate for a practical chemical sensor in addition to a scalable high-quality interconnect.

CHAPTER 5. CONCLUSION

The transport properties of sidewall epiGNR were measured in two separate experiments. The first device design involved superconducting Al contacts as a means of studying the proximity effect in the epiGNR channel. The second experiment measured the electrical noise in epiGNR as a function of gate voltage using a signal analyzer. Both experiments indicated the presence of scattering in the channel and attempts were made to characterize this scattering in depth. These efforts are driven by previous observations of a spin-polarized ground state in the ribbon as well as an interest in epiGNR as a high quality interconnect.

The superconducting proximity effect was established at an Al/Pd/epiGNR interface. Sweeping the magnetic field revealed a clear and abrupt superconducting transition at finite magnetic field. By stepping the bias voltage across epiGNR through a series of values, the reverse proximity effect and a sharp zero bias conductance peak were observed. An extended BTK model was invoked as a means of interpreting the measured conductance spectra. The sharpness of the zero-bias peak was indicative of scattering in the epiGNR channel that amplified the Andreev reflection probability. While this complication limits the quantitative application of the extended BTK model in determining the spin polarization of epiGNR, the role Andreev reflection plays in the positive zero bias conductance peak defies the predicted behavior of a half-metal.

The superconducting signal can be improved in a straightforward manner by either using a dilution fridge to lower the temperature or using a higher T_C superconductor to further differentiate between the Δ_{SC} and $k_B T$ energy scales.

Maintaining a ballistic channel throughout fabrication, as well as reducing the distance between superconducting contacts and reducing the number of epiGNR side branches would help mitigate scattering in the channel such that the Andreev reflection can be quantitatively analyzed and the spin polarization of the epiGNR channel can be determined.

The noise spectral density of an epiGNR device was measured as a function of source-drain, gate voltage, and temperature. The noise amplitude was explored as an extrinsic quantity, independent of the bias or the measurement frequency. Sweeping the gate voltage revealed the CNP along with several transport characteristics of the measured epiGNR device: $\mu = 2066$ $cm^2V^{-1}s^{-1}$, $n_{imp} \approx 5 \times 10^{-11} cm^{-2}$, $A = 4 - 10 \times 10^{-8}$, and $\alpha_H \approx 10^{-4}$. These quantities were compared with several other carbon-based systems and the potential for epiGNR as a high quality interconnect was confirmed. The characteristic 'M' shape of the noise as a function of gate voltage was analyzed and long-range scatterers were found to be the dominant source of scattering in the channel than short-range scatterers. Charged contaminants trapped at the epiGNR/Al_2O_3 interface as a result of the fabrication process were presumed to be the source of this $1/f$ noise.

Reducing the noise level in top-gated epiGNR would be most effectively done by improving the dielectric deposition process. Using atomic layer deposition or an oxygen injection system in the electron-beam evaporator in place of atmospheric oxidation would surely reduce the contaminants at the epiGNR/Al_2O_3 interface and thereby lower the noise amplitude. Patterning the source and drain contacts also introduces contaminants, so a cleaner lithography process (such as shadow deposition) would also improve the

noise characteristics of the device. A thinner ribbon would introduce significant quantum confinement and it may be possible to explore the epiGNR subbands using the noise characteristics of the device [133].

Gating an epiGNR superconducting proximity effect device would allow us to freely move the Fermi level between the spin-polarized ground state and the unpolarized states in high-energy subbands. By comparing the normalized conductance spectra near to the CNP with the spectra far away from the CNP, we could clearly observe the difference in superconducting proximity effect imposed by the spin polarization of the ground state in epiGNR.

Transport devices using epiGNR as a novel conduction channel show great promise for future integrated electronics. With competitive low-frequency noise characteristics, high mobility, ability to be patterned on-chip, and exotic transport properties such as spin polarization, epiGNR has a vast potential for a high-quality transmission line and integrated device components. The work done in this dissertation will be instrumental in improving device fabrication as well as characterizing the exotic properties of epiGNR.

REFERENCES

1 Ashcroft, N. W. & Mermin, N. D. *Solid state physics*. (Holt, 1976).

2 Datta, S. *Electronic Transport in Mesoscopic Systems*. (Cambridge University Press, 1995).

3 *International Technology Roadmap for Semiconductors 2.0.* Atlanta, GA, 2015.

4 Moore, G. The Future of Integrated Electronics. *Electronics Magazine* **38**, 8 (1965).

5 Dutta, S. & Pati, S. K. Novel properties of graphene nanoribbons: a review. *Journal of Materials Chemistry* **20**, 8207 (2010).

6 Nakada, K., Fujita, M., Dresselhaus, G. & Dresselhaus, M. S. Edge state in graphene ribbons: Nanometer size effect and edge shape dependence. *Physical Review B* **54**, 17954-17961 (1996).

7 Wallace, P. R. The Band Theory of Graphite. *Physical Review* **71**, 622-634 (1947).

8 Baringhaus, J., Ruan, M., Edler, F., Tejeda, A., Sicot, M., Taleb-Ibrahimi, A., Li, A. P., Jiang, Z., Conrad, E. H., Berger, C., Tegenkamp, C. & de Heer, W. A. Exceptional ballistic transport in epitaxial graphene nanoribbons. *Nature* **506**, 349-354 (2014).

9 Son, Y. W., Cohen, M. L. & Louie, S. G. Half-metallic graphene nanoribbons. *Nature* **444**, 347-349 (2006).

10 Han, M. Y., Ozyilmaz, B., Zhang, Y. & Kim, P. Energy band-gap engineering of graphene nanoribbons. *Phys Rev Lett* **98**, 206805 (2007).

11 Han, M. Y., Brant, J. C. & Kim, P. Electron transport in disordered graphene nanoribbons. *Phys Rev Lett* **104**, 056801 (2010).

12 Han, M., Ozyilmaz, B., Zhang, Y., Jarillo-Herero, P. & Kim, P. Electronic transport measurements in graphene nanoribbons. *Physica Status Solidi (b)* **244**, 4134-4137 (2007).

13 de Heer, W. A., Berger, C., Ruan, M., Sprinkle, M., Li, X., Hu, Y., Zhang, B., Hankinson, J. & Conrad, E. Large area and structured epitaxial graphene produced by confinement controlled sublimation of silicon carbide. *Proceedings of the National Academy of Sciences of the United States of America* **108**, 16900-16905 (2011).

14 Ruan, M., Hu, Y., Guo, Z., Dong, R., Palmer, J., Hankinson, J., Berger, C., de Heer, W. A., Chakraborty, P. S., Lourenco, N. & Cressler, J. in *International Semiconductor Conference Dresden-Grenoble* (2012).

15 de Heer, W. A. Epitaxial graphene: A new electronic material for the 21st century. *MRS Bulletin* **36**, 632-639 (2011).

16 Sprinkle, M., Ruan, M., Hu, Y., Hankinson, J., Rubio-Roy, M., Zhang, B., Wu, X., Berger, C. & de Heer, W. A. Scalable templated growth of graphene nanoribbons on SiC. *Nat Nanotechnol* **5**, 727-731 (2010).

17 Ruan, M., Hu, Y., Guo, Z., Dong, R., Palmer, J., Hankinson, J., Berger, C. & de Heer, W. A. Epitaxial graphene on silicon carbide: Introduction to structured graphene. *MRS Bulletin* **37**, 1138-1147 (2012).

18 Celis, A., Nair, M. N., Taleb-Ibrahimi, A., Conrad, E. H., Berger, C., de Heer, W. A. & Tejeda, A. Graphene nanoribbons: fabrication, properties and devices. *Journal of Physics D: Applied Physics* **49**, 143001 (2016).

19 Berger, C., Deniz, D., Gigliotti, J., Palmer, J., Hankinson, J., Hu, Y. H., Turmaud, J.-P., Puybaret, R., Ougazzaden, A., Sidorov, A., Jiang, Z. & de Heer, W. A. in *Graphene Growth on Semiconductors* (PanStanford Publishing, 2016).

20 Palacio, I., Celis, A., Nair, M. N., Gloter, A., Zobelli, A., Sicot, M., Malterre, D., Nevius, M. S., de Heer, W. A., Berger, C., Conrad, E. H., Taleb-Ibrahimi, A. & Tejeda, A. Atomic structure of epitaxial graphene sidewall nanoribbons: flat graphene, miniribbons, and the confinement gap. *Nano Lett* **15**, 182-189 (2015).

21 Nevius, M. S., Wang, F., Mathieu, C., Barrett, N., Sala, A., Mentes, T. O., Locatelli, A. & Conrad, E. H. The bottom-up growth of edge specific graphene nanoribbons. *Nano Lett* **14**, 6080-6086 (2014).

22 Nevius, M. S., Conrad, M., Wang, F., Celis, A., Nair, M. N., Taleb-Ibrahimi, A., Tejeda, A. & Conrad, E. H. Semiconducting Graphene from Highly Ordered Substrate Interactions. *Phys Rev Lett* **115**, 136802 (2015).

23 Goler, S., Coletti, C., Piazza, V., Pingue, P., Colangelo, F., Pellegrini, V., Emtsev, K. V., Forti, S., Starke, U., Beltram, F. & Heun, S. Revealing the atomic structure of the buffer layer between SiC(0001) and epitaxial graphene. *Carbon* **51**, 249-254 (2013).

24 Berger, C., Song, Z., Li, T., Li, X., Ogbazghi, A. Y., Feng, R., Dai, Z., Marchenkov, A. N., Conrad, E. H., First, P. N. & de Heer, W. A. Ultrathin Epitaxial Graphite: 2D Electron Gas Properties and a Route toward Graphene-based Nanoelectronics. *The Journal of Physical Chemistry B* **108**, 19912-19916 (2004).

25 Novoselov, K. S., Geim, A. K., Morozov, S. V., Jiang, D., Zhang, Y., Dubonos, S. V., Grigorieva, I. V. & Firsov, A. A. Electric field effect in atomically thin carbon films. *Science* **306**, 666-669 (2004).

26 Berger, C., Song, Z., Li, X., Wu, X., Brown, N., Naud, C., Mayou, D., Li, T., Hass, J., Marchenkov, A. N., Conrad, E. H., First, P. N. & de Heer, W. A. Electronic confinement and coherence in patterned epitaxial graphene. *Science* **312**, 1191-1196 (2006).

27 Geim, A. K. & Novoselov, K. S. The rise of graphene. *Nat Mater* **6**, 183-191 (2007).

28 Novoselov, K. S., Fal'ko, V. I., Colombo, L., Gellert, P. R., Schwab, M. G. & Kim, K. A roadmap for graphene. *Nature* **490**, 192-200 (2012).

29 Nair, R. R., Blake, P., Grigorenko, A. N., Novoselov, K. S., Booth, T. J., Stauber, T., Peres, N. M. & Geim, A. K. Fine structure constant defines visual transparency of graphene. *Science* **320**, 1308 (2008).

30 Bolotin, K. I., Ghahari, F., Shulman, M. D., Stormer, H. L. & Kim, P. Observation of the fractional quantum Hall effect in graphene. *Nature* **462**, 196-199 (2009).

31 Du, X., Skachko, I., Duerr, F., Luican, A. & Andrei, E. Y. Fractional quantum Hall effect and insulating phase of Dirac electrons in graphene. *Nature* **462**, 192-195 (2009).

32 Schedin, F., Geim, A. K., Morozov, S. V., Hill, E. W., Blake, P., Katsnelson, M. I. & Novoselov, K. S. Detection of individual gas molecules adsorbed on graphene. *Nat Mater* **6**, 652-655 (2007).

33 Dobson, J. F., White, A. & Rubio, A. Asymptotics of the dispersion interaction: analytic benchmarks for van der Waals energy functionals. *Phys Rev Lett* **96**, 073201 (2006).

34 Morozov, S. V., Novoselov, K. S., Katsnelson, M. I., Schedin, F., Elias, D. C., Jaszczak, J. A. & Geim, A. K. Giant intrinsic carrier mobilities in graphene and its bilayer. *Phys Rev Lett* **100**, 016602 (2008).

35 Chen, J. H., Cullen, W. G., Jang, C., Fuhrer, M. S. & Williams, E. D. Defect scattering in graphene. *Phys Rev Lett* **102**, 236805 (2009).

36 Robinson, J. A., Wetherington, M., Tedesco, J. L., Campbell, P. M., Weng, X., Stitt, J., Fanton, M. A., Frantz, E., Snyder, D., VanMil, B. L., Jernigan, G. G., Myers-Ward, R. L., Eddy, C. R., Jr. & Gaskill, D. K. Correlating Raman spectral signatures with carrier mobility in epitaxial graphene: a guide to achieving high mobility on the wafer scale. *Nano Lett* **9**, 2873-2876 (2009).

37 Butler, W. H. Tunneling magnetoresistance from a symmetry filtering effect. *Science and Technology of Advanced Materials* **9**, 014106 (2016).

38 Julliere, M. Tunneling between ferromagnetic films. *Physics Letters A* **54**, 225-226 (1975).

39 Hankinson, J. *Spin Dependent Current Injection Into Epitaxial Graphene Nanoribbons* PhD thesis, Georgia Tech, (2015).

40 Tehrani, S., Slaughter, J. M., Chen, E., Durlam, M., Shi, J. & DeHerren, M. Progress and outlook for MRAM technology. *IEEE Transactions on Magnetics* **35**, 2814-2819 (1999).

41 Campbell, S. A. *Fabrication Engineering at the Micro and Nanoscale*. 3rd edn, (Oxford University Press, 2007).

42 Her, M., Beams, R. & Novotny, L. Graphene transfer with reduced residue. *Physics Letters A* **377**, 1455-1458 (2013).

43 Howard, R. E., Hu, E. L. & Jackel, L. D. Multilevel resist for lithography below 100 nm. *IEEE Transactions on Electron Devices* **28**, 1378-1381 (1981).

44 Sugiura, J. Reactive ion etching of SiC thin films using fluorinated gases. *Journal of Vacuum Science & Technology B: Microelectronics and Nanometer Structures* **4**, 349 (1986).

45 Palmer, J., Kunc, J., Hu, Y., Hankinson, J., Guo, Z., Berger, C. & de Heer, W. A. Controlled epitaxial graphene growth within removable amorphous carbon corrals. *Applied Physics Letters* **105**, 023106 (2014).

46 Graf, D., Molitor, F., Ensslin, K., Stampfer, C., Jungen, A., Hierold, C. & Wirtz, L. Spatially resolved Raman spectroscopy of single- and few-layer graphene. *Nano Lett* **7**, 238-242 (2007).

47 Renault, O., Pascon, A. M., Rotella, H., Kaja, K., Mathieu, C., Rault, J. E., Blaise, P., Poiroux, T., Barrett, N. & Fonseca, L. R. C. Charge spill-out and work function of few-layer graphene on SiC(0 0 0 1). *Journal of Physics D: Applied Physics* **47**, 295303 (2014).

48 Rodriguez, B. J., Yang, W. C., Nemanich, R. J. & Gruverman, A. Scanning probe investigation of surface charge and surface potential of GaN-based heterostructures. *Applied Physics Letters* **86**, 112115 (2005).

49 Kellar, J. A., Alaboson, J. M. P., Wang, Q. H. & Hersam, M. C. Identifying and characterizing epitaxial graphene domains on partially graphitized SiC(0001) surfaces using scanning probe microscopy. *Applied Physics Letters* **96**, 143103 (2010).

50 Childres, I., Jauregui, L. A., Tian, J. & Chen, Y. P. Effect of oxygen plasma etching on graphene studied using Raman spectroscopy and electronic transport measurements. *New Journal of Physics* **13**, 025008 (2011).

51 Sree Harsha, K. S. *Principles of Vapor Deposition of Thin Films*. 367-452 (Elsevier Science, 2005).

52 Seshan, K. *Handbook of Thin Film Deposition Processes and Techniques*. 2nd edn, (William Andrew Publishing/Noyes, 2002).

53 Ames, I. Crucible Type Evaporation Source for Aluminum. *Review of Scientific Instruments* **37**, 1737 (1966).

54 Mann, D., Javey, A., Kong, J., Wang, Q. & Dai, H. Ballistic Transport in Metallic Nanotubes with Reliable Pd Ohmic Contacts. *Nano Lett* **3**, 1541-1544 (2003).

55 Xia, F., Perebeinos, V., Lin, Y. M., Wu, Y. & Avouris, P. The origins and limits of metal-graphene junction resistance. *Nat Nanotechnol* **6**, 179-184 (2011).

56 Santhanam, P., Wind, S. & Prober, D. E. Localization, superconducting fluctuations, and superconductivity in thin films and narrow wires of aluminum. *Physical Review B* **35**, 3188-3206 (1987).

57 Kölbel, M., Tjerkstra, R. W., Brugger, J., van Rijn, C. J. M., Nijdam, W., Huskens, J. & Reinhoudt, D. N. Shadow-Mask Evaporation through Monolayer-Modified Nanostencils. *Nano Lett* **2**, 1339-1343 (2002).

58 Campbell, T., Kalia, R. K., Nakano, A., Vashishta, P., Ogata, S. & Rodgers, S. Dynamics of Oxidation of Aluminum Nanoclusters using Variable Charge Molecular-Dynamics Simulations on Parallel Computers. *Physical Review Letters* **82**, 4866-4869 (1999).

59 de Jong, M. J. & Beenakker, C. W. Andreev reflection in ferromagnet-superconductor junctions. *Phys Rev Lett* **74**, 1657-1660 (1995).

60 Soulen Jr, R. J. Measuring the Spin Polarization of a Metal with a Superconducting Point Contact. *Science* **282**, 85-88 (1998).

61 Upadhyay, S. K., Palanisami, A., Louie, R. N. & Buhrman, R. A. Probing Ferromagnets with Andreev Reflection. *Physical Review Letters* **81**, 3247-3250 (1998).

62 Ji, Y., Strijkers, G. J., Yang, F. Y., Chien, C. L., Byers, J. M., Anguelouch, A., Xiao, G. & Gupta, A. Determination of the spin polarization of half-metallic CrO(2) by point contact Andreev reflection. *Phys Rev Lett* **86**, 5585-5588 (2001).

63 Panguluri, R. P., Nadgorny, B., Wojtowicz, T., Lim, W. L., Liu, X. & Furdyna, J. K. Measurement of spin polarization by Andreev reflection in ferromagnetic In1−xMnxSb epilayers. *Applied Physics Letters* **84**, 4947-4949 (2004).

64 Jiang, Z., Aumentado, J., Belzig, W. & Chandrasekhar, V. *St. Petersburg NATO Conference on Quantum transport.* St. Petersburg, 2003.

65 Bardeen, J., Cooper, L. N. & Schrieffer, J. R. Microscopic Theory of Superconductivity. *Physical Review* **106**, 162-164 (1957).

66 London, F. & London, H. The electromagnetic equations of the supraconductor. *Proc R Soc Lon Ser-A* **149**, 0071-0088 (1935).

67 Leggett, A. J. What DO we know about high Tc? *Nature Physics* **2**, 134-136 (2006).

68 Kamerlingh Onnes, H. Further experiments with liquid helium. C. On the change of electric resistance of pure metals at very low temperatures, etc. IV. The resistance of pure mercury at helium temperatures. *Comm. Phys. Lab. Univ. Leiden* **120b** (1911).

69 Andreev, A. F. The Thermal Conductivity of the Intermediate State in Superconductors. *Soviet Physics Jetp-Ussr* **19**, 1228-1231 (1964).

70 Edwards, J. T. & Thouless, D. J. Numerical studies of localization in disordered systems. *Journal of Physics C: Solid State Physics* **5**, 807-820 (1972).

71 Josephson, B. D. The discovery of tunnelling supercurrents. *Reviews of Modern Physics* **46**, 251-254 (1974).

72 Heersche, H. B., Jarillo-Herrero, P., Oostinga, J. B., Vandersypen, L. M. & Morpurgo, A. F. Bipolar supercurrent in graphene. *Nature* **446**, 56-59 (2007).

73 Pallecchi, E., Gaaß, M., Ryndyk, D. A. & Strunk, C. Carbon nanotube Josephson junctions with Nb contacts. *Applied Physics Letters* **93**, 072501 (2008).

74 Ishida, K., Mukuda, H., Kitaoka, Y., Asayama, K., Mao, Z. Q., Mori, Y. & Maeno, Y. Spin-triplet superconductivity in Sr2RuO4 identified by 17O Knight shift. *Nature* **396**, 658-660 (1998).

75 Morpurgo, A. F. Gate-Controlled Superconducting Proximity Effect in Carbon Nanotubes. *Science* **286**, 263-265 (1999).

76 Blonder, G. E., Tinkham, M. & Klapwijk, T. M. Transition from metallic to tunneling regimes in superconducting microconstrictions: Excess current, charge imbalance, and supercurrent conversion. *Physical Review B* **25**, 4515-4532 (1982).

77 Meissner, W. & Ochsenfeld, R. Ein neuer Effekt bei Eintritt der Supraleitfahigkeit. *Die Naturwissenschaften* **21**, 787-788 (1933).

78 London, F. On the Problem of the Molecular Theory of Superconductivity. *Physical Review* **74**, 562-573 (1948).

79 Meservey, R. & Tedrow, P. M. Spin-polarized electron tunneling. *Physics Reports* **238**, 173-243 (1994).

80 Ji., Y. in *ProQuest Dissertations and Thesis* Vol. 64-01 B (ed The Johns Hopkins University) 773 (2003).

81 McCann, E., Kechedzhi, K., Fal'ko, V. I., Suzuura, H., Ando, T. & Altshuler, B. L. Weak-localization magnetoresistance and valley symmetry in graphene. *Phys Rev Lett* **97**, 146805 (2006).

82 Wu, X., Li, X., Song, Z., Berger, C. & de Heer, W. A. Weak antilocalization in epitaxial graphene: evidence for chiral electrons. *Phys Rev Lett* **98**, 136801 (2007).

83 Shin, Y. J., Kwon, J. H., Kalon, G., Lam, K.-T., Bhatia, C. S., Liang, G. & Yang, H. Ambipolar bistable switching effect of graphene. *Applied Physics Letters* **97**, 262105 (2010).

84 Ceric, H. & Selberherr, S. Electromigration in submicron interconnect features of integrated circuits. *Materials Science and Engineering: R: Reports* **71**, 53-86 (2011).

85 Kittel, C. *Introduction to Solid State Physics*. 5th edn, (John Wiley & Sons, Inc., 1976).

86 Nguyen, C., Kroemer, H. & Hu, E. L. Anomalous Andreev conductance in InAs-AlSb quantum well structures with Nb electrodes. *Phys Rev Lett* **69**, 2847-2850 (1992).

87 van Wees, B. J., de Vries, P., Magnee, P. & Klapwijk, T. M. Excess conductance of superconductor-semiconductor interfaces due to phase conjugation between electrons and holes. *Phys Rev Lett* **69**, 510-513 (1992).

88 Yu, W., Jiang, Y., Huan, C., Chen, X., Jiang, Z., Hawkins, S. D., Klem, J. F. & Pan, W. Superconducting proximity effect in inverted InAs/GaSb quantum well structures with Ta electrodes. *Applied Physics Letters* **105**, 192107 (2014).

89 Ryazanov, V. V., Oboznov, V. A., Rusanov, A. Y., Veretennikov, A. V., Golubov, A. A. & Aarts, J. Coupling of two superconductors through a ferromagnet: evidence for a pi junction. *Phys Rev Lett* **86**, 2427-2430 (2001).

90 Calado, V. E., Goswami, S., Nanda, G., Diez, M., Akhmerov, A. R., Watanabe, K., Taniguchi, T., Klapwijk, T. M. & Vandersypen, L. M. Ballistic Josephson junctions in edge-contacted graphene. *Nat Nanotechnol* **10**, 761-764 (2015).

91 Tombros, N., Veligura, A., Junesch, J., Guimarães, M. H. D., Vera-Marun, I. J., Jonkman, H. T. & van Wees, B. J. Quantized conductance of a suspended graphene nanoconstriction. *Nature Physics* **7**, 697-700 (2011).

92 Liu, F., Bao, M., Kim, H.-j., Wang, K. L., Li, C., Liu, X. & Zhou, C. Giant random telegraph signals in the carbon nanotubes as a single defect probe. *Applied Physics Letters* **86**, 163102 (2005).

93 Wong, H. Low-frequency noise study in electron devices: review and update. *Microelectronics Reliability* **43**, 585-599 (2003).

94 Balandin, A. A. Low-frequency 1/f noise in graphene devices. *Nat Nanotechnol* **8**, 549-555 (2013).

95 Robinson, J. T., Perkins, F. K., Snow, E. S., Wei, Z. & Sheehan, P. E. Reduced graphene oxide molecular sensors. *Nano Lett* **8**, 3137-3140 (2008).

96 Johnson, J. B. Thermal Agitation of Electricity in Conductors. *Physical Review* **32**, 97-109 (1928).

97 Nyquist, H. Thermal Agitation of Electric Charge in Conductors. *Physical Review* **32**, 110-113 (1928).

98 McWhorter, A. L. *Semiconductor Surface Physics*. (University of Pennsylvania Press, 1956).

99 Liu, G., Rumyantsev, S., Shur, M. S. & Balandin, A. A. Origin of 1/f noise in graphene multilayers: Surface vs. volume. *Applied Physics Letters* **102**, 093111 (2013).

100 Collins, P. G., Fuhrer, M. S. & Zettl, A. 1/f noise in carbon nanotubes. *Applied Physics Letters* **76**, 894 (2000).

101 Chen, Z., Lin, Y.-M., Rooks, M. J. & Avouris, P. Graphene nano-ribbon electronics. *Physica E: Low-dimensional Systems and Nanostructures* **40**, 228-232 (2007).

102 Lee, S. K., Kang, C. G., Lee, Y. G., Cho, C., Park, E., Chung, H. J., Seo, S., Lee, H.-D. & Lee, B. H. Correlation of low frequency noise characteristics with the interfacial charge exchange reaction at graphene devices. *Carbon* **50**, 4046-4051 (2012).

103 Grandchamp, B., Fregonese, S., Majek, C., Hainaut, C., Maneux, C., Meng, N., Happy, H. & Zimmer, T. Characterization and Modeling of Graphene Transistor

Low-Frequency Noise. *IEEE Transactions on Electron Devices* **59**, 516-519 (2012).

104 Stolyarov, M. A., Liu, G., Rumyantsev, S. L., Shur, M. & Balandin, A. A. Suppression of 1/f noise in near-ballistic h-BN-graphene-h-BN heterostructure field-effect transistors. *Applied Physics Letters* **107**, 023106 (2015).

105 Xu, G., Torres, C. M., Jr., Zhang, Y., Liu, F., Song, E. B., Wang, M., Zhou, Y., Zeng, C. & Wang, K. L. Effect of spatial charge inhomogeneity on 1/f noise behavior in graphene. *Nano Lett* **10**, 3312-3317 (2010).

106 Kaverzin, A. A., Mayorov, A. S., Shytov, A. & Horsell, D. W. Impurities as a source of1/f noise in graphene. *Physical Review B* **85**, 075435 (2012).

107 Zhang, Y., Mendez, E. E. & Du, X. Mobility-Dependent Low-Frequency Noise in Graphene Field-Effect Transistors. *ACS Nano* **5**, 7 (2011).

108 Li, X., Lu, X., Li, T., Yang, W., Fang, J., Zhang, G. & Wu, Y. Noise in Graphene Superlattices Grown on Hexagonal Boron Nitride. *ACS Nano* **9**, 11382-11388 (2015).

109 Qinghui, S., Guanxiong, L., Teweldebrhan, D., Balandin, A. A., Rumyantsev, S., Shur, M. S. & Dong, Y. Flicker Noise in Bilayer Graphene Transistors. *IEEE Electron Device Letters* **30**, 288-290 (2009).

110 Lin, Y. M. & Avouris, P. Strong suppression of electrical noise in bilayer graphene nanodevices. *Nano Lett* **8**, 2119-2125 (2008).

111 Liu, G., Stillman, W., Rumyantsev, S., Shao, Q., Shur, M. & Balandin, A. A. Low-frequency electronic noise in the double-gate single-layer graphene transistors. *Applied Physics Letters* **95**, 033103 (2009).

112 Hooge, F. N. 1/f Noise. *Physica* **83B**, 14-23 (1976).

113 Tobias, D., Ishigami, M., Tselev, A., Barbara, P., Williams, E. D., Lobb, C. J. & Fuhrer, M. S. Origins of1⁄f noise in individual semiconducting carbon nanotube field-effect transistors. *Physical Review B* **77** (2008).

114 Pal, A. N. & Ghosh, A. Ultralow noise field-effect transistor from multilayer graphene. *Applied Physics Letters* **95**, 082105 (2009).

115 Yu, Y. J., Zhao, Y., Ryu, S., Brus, L. E., Kim, K. S. & Kim, P. Tuning the graphene work function by electric field effect. *Nano Lett* **9**, 3430-3434 (2009).

116 Li, X., Wu, X., Sprinkle, M., Ming, F., Ruan, M., Hu, Y., Berger, C. & de Heer, W. A. Top- and side-gated epitaxial graphene field effect transistors. *Physica Status Solidi (a)* **207**, 286-290 (2010).

117 Palmer, H. B. The Capacitance of a Parallel-Plate Capacitor by the Schwartz-Christoffel Transformation. *Transactions of the American Institute of Electrical Engineers* **56**, 363-366 (1937).

118 Nyquist, H. Certain Topics in Telegraph Transmission Theory. *Transactions of the American Institute of Electrical Engineers* **47**, 617-644 (1928).

119 Ruan, M. *Structured epitaxial graphene for electronics* PhD thesis, Georgia Tech, (2012).

120 Suk, J. W., Lee, W. H., Lee, J., Chou, H., Piner, R. D., Hao, Y., Akinwande, D. & Ruoff, R. S. Enhancement of the electrical properties of graphene grown by chemical vapor deposition via controlling the effects of polymer residue. *Nano Lett* **13**, 1462-1467 (2013).

121 Kim, S., Nah, J., Jo, I., Shahrjerdi, D., Colombo, L., Yao, Z., Tutuc, E. & Banerjee, S. K. Realization of a high mobility dual-gated graphene field-effect transistor with Al2O3 dielectric. *Applied Physics Letters* **94**, 062107 (2009).

122 Postma, H. W. C., Teepen, T. F., Yao, Z. & Dekker, C. 1/f noise in carbon nanotubes. *Electronic Correlations: From Meso- to Nano-Physics*, 433-436 (2001).

123 Guo, Z. *Mono-layer C-Face Epitaxial Graphene For High Frequency Electronics* PhD thesis, Georgia Tech, (2014).

124 Adam, S., Hwang, E. H., Rossi, E. & Das Sarma, S. Theory of charged impurity scattering in two-dimensional graphene. *Solid State Communications* **149**, 1072-1079 (2009).

125 Chung, H.-J., Woo Uhm, T., Won Kim, S., Gyu You, Y., Wook Lee, S., Ho Jhang, S., Campbell, E. E. B. & Woo Park, Y. Random telegraph noise in metallic single-walled carbon nanotubes. *Applied Physics Letters* **104**, 193102 (2014).

126 Rossi, E. & Das Sarma, S. Ground state of graphene in the presence of random charged impurities. *Phys Rev Lett* **101**, 166803 (2008).

127 Hwang, E. H., Adam, S. & Sarma, S. D. Carrier transport in two-dimensional graphene layers. *Phys Rev Lett* **98**, 186806 (2007).

128 Mayorov, A. S., Gorbachev, R. V., Morozov, S. V., Britnell, L., Jalil, R., Ponomarenko, L. A., Blake, P., Novoselov, K. S., Watanabe, K., Taniguchi, T. & Geim, A. K. Micrometer-scale ballistic transport in encapsulated graphene at room temperature. *Nano Lett* **11**, 2396-2399 (2011).

129 Balandin, A., Wang, K. L., Svizhenko, A. & Bandyopadhyay, S. The fundamental 1/f noise and the Hooge parameter in semiconductor quantum wires. *IEEE Transactions on Electron Devices* **46**, 1240-1244 (1999).

130 Lin, Y. M., Appenzeller, J., Knoch, J., Chen, Z. & Avouris, P. Low-frequency current fluctuations in individual semiconducting single-wall carbon nanotubes. *Nano Lett* **6**, 930-936 (2006).

131 Snow, E. S., Novak, J. P., Lay, M. D. & Perkins, F. K. 1/f noise in single-walled carbon nanotube devices. *Applied Physics Letters* **85**, 4172-4174 (2004).

132 Rumyantsev, S., Liu, G., Shur, M. S., Potyrailo, R. A. & Balandin, A. A. Selective gas sensing with a single pristine graphene transistor. *Nano Lett* **12**, 2294-2298 (2012).

133 Xu, G., Torres, C. M., Song, E. B., Tang, J., Bai, J., Duan, X., Zhang, Y. & Wang, K. L. Enhanced conductance fluctuation by quantum confinement effect in graphene nanoribbons. *Nano Lett* **10**, 4590-4594 (2010).